Effects of Heating and Cooling Rates on Phase Transformations in 10 Wt Pct Ni Steel and Their Application to Gas Tungsten Arc Welding

ERIN J. BARRICK, DIVYA JAIN, JOHN N. DUPONT, and DAVID N. SEIDMAN

10 wt pct Ni steel is a high-strength steel that possesses good ballistic resistance from the deformation induced transformation of austenite to martensite, known as the transformation-induced-plasticity effect. The effects of rapid heating and cooling rates associated with welding thermal cycles on the phase transformations and microstructures, specifically in the heat-affected zone, were determined using dilatometry, microhardness, and microstructural characterization. Heating rate experiments demonstrate that the Ac_3 temperature is dependent on heating rate, varying from 1094 K (821 °C) at a heating rate of 1 °C/s to 1324 K (1051 °C) at a heating rate of 1830 °C/s. A continuous cooling transformation diagram produced for 10 wt pct Ni steel reveals that martensite will form over a wide range of cooling rates, which reflects a very high hardenability of this alloy. These results were applied to a single pass, autogenous, gas tungsten arc weld. The diffusion of nickel from regions of austenite to martensite during the welding thermal cycle manifests itself in a muddled, rod-like lath martensitic microstructure. The results of these studies show that the nickel enrichment of the austenite in 10 wt pct Ni steel plays a critical role in phase transformations during welding.

I. INTRODUCTION

NAVAL applications require the use of steels with high strength and high toughness over a wide range of welding and service conditions. A 10 wt pct Ni steel has been developed with ballistic resistance, strength, and toughness values exceeding those of steels currently used, and is now being considered as a candidate material to replace existing high strength, low alloy steels.[1] The yield strength in the optimally heat-treated condition is 908 MPa and the Charpy impact toughness at 189 K (− 84 °C) is 147 J,[1] thus demonstrating that this steel meets the low temperature toughness requirements for the intended application. The steel obtains high strength from the formation of martensite and good toughness from the addition of nickel and the concomitant, associated mechanically induced transformation of austenite to martensite, known as the transformation-induced-plasticity (TRIP) phenomenon.[1,2]

For some time, the achievement of simultaneous high strength and toughness in TRIP steels has been understood.[3] The progressive formation of martensite in the presence of stress or strain causes a higher rate of work hardening and relieves stress concentrations; the resulting outcomes are increases in strength, ductility, and toughness.[4,5] To accomplish this, the alloy content and thermomechanical treatments are designed to stabilize austenite at room temperature. The success of the TRIP principle hinges on the stability and volume fraction of austenite present, which is determined by the composition and heat treatment. This 10 wt pct Ni steel obtains the necessary austenite for the TRIP mechanism through a three-step quenching, lamellarization, and tempering (QLT) heat treatment. QLT heat treatments were originally developed for lower-Ni steel such as 5.5 wt pct Ni steel, but have been adapted for higher Ni content steels in the last 20 years.[6–14] The quenching step (Q) involves heating in the single phase γ region, and both the lamellarization step (L) and tempering treatment (T) are conducted between the Ac_1 and Ac_3 temperatures in the two-phase $(\alpha + \gamma)$ field.[12] The Q treatment is responsible for generating a lath martensite microstructure, which provides high strength of the alloy.[6] During the L treatment, austenite forms on the

ERIN J. BARRICK and JOHN N. DUPONT are with the Lehigh University, 5 East Packer Ave, Bethlehem, PA, 18015. Contact e-mail: ejb314@lehigh.edu DIVYA JAIN is with the Department of Materials Science & Engineering, Northwestern University, 2220 Campus Drive, Evanston, IL, 60208. DAVID N. SEIDMAN is with the Department of Materials Science & Engineering, Northwestern University, and also with the Northwestern University Center for Atom-Probe Tomography (NUCAPT), 2220 Campus Drive, Evanston, IL, 60208.

prior austenite grain boundaries and/or the martensite lath boundaries and becomes enriched in austenite-stabilizing elements. However, some of the austenite formed at this stage is not thermally stable, so upon quenching, some austenite transforms to as-quenched martensite still enriched in the austenite-stabilizing elements.[11,13,15] After the L treatment, the microstructure consists of tempered lath martensite that did not transform to austenite during the L treatment, as-quenched martensite that is compositionally enriched in austenite-stabilizing elements, such as C, Ni, and Mn, and austenite.[15] Since the as-quenched martensite is rich in austenite-stabilizing elements, it has a lower Ac_1 temperature than the tempered martensite. Thus, during the T treatment, it transforms to austenite, and with continued diffusion of the stabilizing elements during the T treatment, the austenite avoids transformation to martensite during cooling.[11,13] Research on the optimally QLT heat-treated 10 wt pct Ni steel reveals that the microstructure consists of tempered lath martensite, 15 to 20 vol pct austenite enriched in Ni, Mn, Cu, C, and Cr, and M_2C alloy carbides.[1,2,15] The austenite is located at the lath boundaries, thereby producing fine mixtures of martensite and austenite (M + A) that have a rod-like morphology.[1]

During the construction of naval combatant ships, one of the most important fabrication steps is fusion welding. As has been discussed, this steel requires a complex heat treatment schedule to maximize the TRIP response and provide excellent mechanical properties. However, fusion welding involves severe thermal and strain cycles that could significantly affect the microstructure of the heat-affected zone (HAZ) and fusion zone, which usually results in a reduction of properties in these areas. Thus, although it has already been proven that this steel has excellent mechanical properties that could provide significant advantages to the steel community, 10 wt pct Ni steel cannot yet be implemented for full scale use. With this challenge of welding thermal cycles in mind, the overall objective for this research is to develop a fundamental understanding of the phase transformations associated with rapid heating and cooling thermal cycles, which are concomitant with fusion welds. This work combines the effects of heating rate and cooling rate on the phase transformations and microstructures in 10 wt pct Ni steel, and applies these results to rationalize the HAZ in a single pass weld of this steel. This current study is confined to investigation of microstructural evolution in the HAZ that, unlike the fusion zone, is not subjected to solidification-induced microsegregation that further complicates the phase transformations on cooling. Work is in progress to investigate microstructural evolution in the fusion zone and will be reported in future work.

II. EXPERIMENTAL PROCEDURE

Plates of 10 wt pct Ni steel were received from the Naval Surface Warfare Center, Carderock Division. The plates were heat treated with the optimal QLT heat treatment: Q—1053 K (780 °C) for 1 hour followed by water quenching, L—923 K (650 °C) for 30 minutes followed by water quenching, and T—863 K (590 °C) for 1 hour followed by water quenching. The chemical composition as measured by optical emission spectroscopy is shown in Table I. The volume fraction of the austenite in the QLT treated sample was measured using X-ray diffraction (XRD). A sample of the base metal was sectioned to be ~2 mm thick and was metallographically prepared to a 1 μm diamond polish. XRD was performed using a Scintag XDS2000 diffractometer with a Cu Kα (λ = 0.154 nm) radiation source. X-rays were acquired using an angular step size of 0.05 deg and a scan rate of 0.01°/min for a range of 48 to 93 deg, such that three austenite (FCC) peaks and two martensite (BCC) peaks were acquired. Quantitative analysis of the austenite was performed with the DMSNT software package, version 1.37 (Scintag, Inc.), using the comparison method,[16] which compares the intensities of XRD peaks for austenite and martensite. Each peak was fitted using a Pearson VII function after the background was subtracted. The measured volume fractions were calibrated with a NIST standard[17] containing 5.8 vol pct austenite, which was measured under the same conditions. The value reported is the average of three XRD scans that were performed.

Heating rate and cooling rate dilatometry experiments were performed in a Gleeble 3500 thermomechanical simulator. Specimens used for testing were 6 mm in diameter and 70 mm in length. These dilatometry experiments in the Gleeble used a linear variable differential transformer dilatometer to measure diameter dilation during heating and cooling. Samples for heating rate experiments were heated at either 1 or 1830 °C/s to a peak temperature of 1273 K or 1523 K (1000 °C or 1250 °C), for a total of four conditions. The 1 °C/s was chosen to represent conditions close to equilibrium. The 1830 °C/s was chosen to represent the upper end of heating rates that could be experienced during welding. By examining both heating rates, a range of austenite transformation temperatures could be determined. All samples for the heating rate experiments were cooled at 10 °C/s. Alongside the heating rate studies, a set of isothermal experiments were performed in the Gleeble. First, a sample was heated at a fast heating rate of 1000 °C/s to a peak temperature of 1198 K (925 °C), held at the peak temperature for 5 seconds, and cooled at 50 °C/s, to provide a baseline sample. Then, another sample was heated at the same heating rate to 1198 K (925 °C), held isothermally for 5 minutes, and then cooled at 50 °C/s. Samples for the cooling rate experiments were heated at 10 °C/s to a peak temperature of 1523 K (1250 °C), where they were held for 5 minutes. The samples were then cooled at four different cooling rates: 50, 10, 1, and 0.1 °C/s. Transformation temperatures upon heating for the heating rate samples and upon cooling for the cooling rate samples were determined by adding lines tangent to the heating/cooling curves. The transformation begins when the slope of the dilation deviates from a linear curve and the transformation ends when the slope returns to linearity. The transformation temperatures were confirmed by calculating the derivative of the dilation as a function of the sample temperature and then observing changes in the

Table I. Composition of 10 Wt Pct Ni Steel

	Fe	C	Ni	Mo	V	Cr	Mn	Si	Cu
Nominal overall (wt pct)	87.04	0.10	9.64	1.53	0.06	0.65	0.64	0.18	0.16
Nominal overall (at. pct)	87.5	0.47	9.22	0.90	0.07	0.70	0.65	0.36	0.14
Martensite (at. pct)	92.4 ± 0.12	0.08 ± 0.01	6.00 ± 0.10	0.24 ± 0.02	0.02 ± 0.006	0.54 ± 0.03	0.29 ± 0.02	0.32 ± 0.02	0.07 ± 0.01
Ni-rich (austenite) (at. pct)	77.73 ± 0.20	0.37 ± 0.03	18.26 ± 0.19	0.31 ± 0.03	0.02 ± 0.01	0.88 ± 0.05	1.64 ± 0.06	0.36 ± 0.03	0.29 ± 0.03

The nominal overall composition was measured by optical emissions spectroscopy. The compositions of martensite and austenite were measured using the local atom probe tomography results in Fig. 2.

slope of the derivative curves. Using this method, the transformation begins when the slope of the derivative of dilation deviates from zero and the transformation ends when the slope returns to zero.

An autogenous (without filler metal), single pass, gas tungsten arc weld (GTAW) was made on a plate of QLT 10 wt pct Ni steel that was 11 mm thick. The welding parameters were: 150 A, 10 V, and a travel speed of 2 mm/s. A second autogenous weld was made to help understand the microstructures in the QLT 10 wt pct Ni weld. A sample of QLT 10 wt pct Ni steel also of 11 mm thickness was heat treated at 1173 K (900 °C) for 1 hour followed by water quenching to produce a microstructure of all as-quenched martensite, thereby eliminating any austenite. An autogenous GTAW, called the as-quenched weld, was made with the following parameters: 150 A, 10.7 V, and a travel speed of 2 mm/s. For interpretation of HAZ microstructures, one Gleeble HAZ simulation was performed. A thermal cycle for a heat input of 1500 J/mm was generated using Sandia's Smartweld program[18,19] for a peak temperature of 823 K (550 °C).

The dilatometry samples and welds were analyzed using light optical microscopy (LOM), scanning electron microscopy (SEM), and microhardness. The welds and dilatometry samples were cross-sectioned and metallographically prepared up through a final polish of 50 nm colloidal silica followed by etching with 2 pct Nital for 8 to 10 seconds. A microhardness map was made on a transverse section of the QLT weld using a Leco LM-248 hardness tester with a 100 g load on a Vickers indenter. Indents for the map were placed in a grid such that indents were horizontally spaced in 200 μm increments and vertically spaced in 500 μm increments. Upon inspection using LOM, the location of the fusion line was identified and superimposed on the map. Microhardness traces were performed on both welds across the fusion zone, HAZ, and base metal to observe minor changes in hardness using a Leco LM-248 hardness tester with a 100 g load on a Vickers indenter, and the indents were spaced in 100 μm increments. Microhardness testing was performed on the dilatometry samples using a 300 g load on a Vickers indenter. Each microhardness value reported is an average of 15 measurements randomly distributed. The welds and dilatometry samples were analyzed in a Hitachi 4300SE/N Schottky field emission SEM operating at 8 to 10 kV in SE mode. To aid with understanding the transformation temperature trends, phase volume fraction calculations were performed using the Thermo-Calc software package[20] version 2015b and the TCFE8 Steels/Fe-alloys database version 8.[21]

Select regions of the HAZ in the QLT weld were chosen for advanced characterization using atom probe tomography (APT). 3D APT nanotips were prepared using dual-beam focused-ion beam microscopy by a standard lift-out technique,[22] and the specific details of the lift-out process are provided in a previous publication of 10 wt pct Ni steel.[2] 3D APT experiments were performed with a Cameca local electrode atom probe (LEAP) 4000X-Si tomograph, using ultraviolet (wavelength = 355 nm) picosecond laser pulsing with an
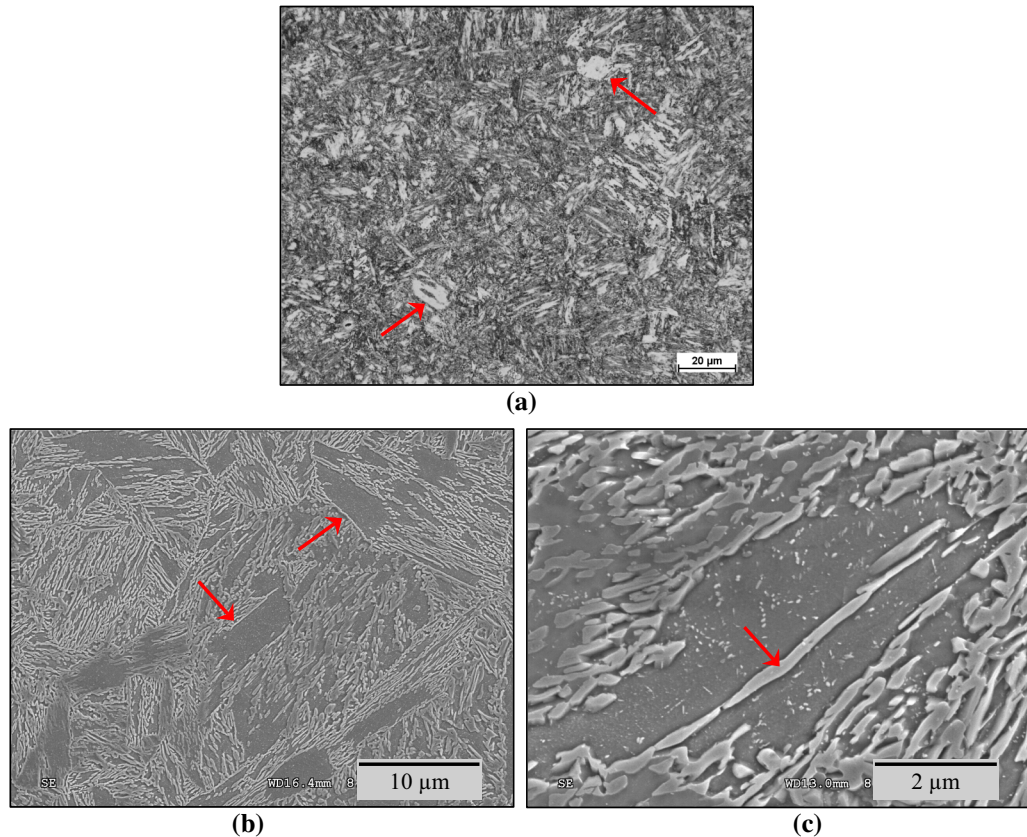
Fig. 1—Microstructure of the base metal. Coarse martensite constituent indicated by arrows. (*a*) Light optical micrograph. (*b*) SEM micrograph of overall microstructure. (*c*) Higher magnification SEM micrograph of coarse martensite constituent.

energy of 30 pJ per pulse, a pulse repetition rate of 500 kHz, and an average evaporation rate (number of ions per pulse) of 2 pct. The samples were analyzed at a specimen base temperature of 60 K in ultrahigh vacuum ($< 10^{-8}$ Pa), and the data obtained were analyzed using the program IVAS 3.6 (Cameca, Madison, WI).

III. RESULTS

A. *Base Metal Characterization*

Figure 1 shows the microstructure of the base metal; Figure 1(a) is a LOM micrograph and Figures 1(b) and (c) are SEM micrographs. The matrix consists of tempered lath martensite, which is consistent with previous investigations of this steel.[1,2] The austenite and alloy carbides cannot be resolved at this level of examination, so they will be discussed using APT below. The microstructure also contains a coarse martensite constituent that was found in a similar 9 wt pct Ni steel.[23] This constituent has been identified as two separate constituents in the literature: coarse autotempered martensite[23–25] and coalesced bainite/martensite.[26–31] While the morphology of these constituents is the same, the proposed mechanism of formation is different. It is beyond the scope of this research to identify the formation process of this constituent; therefore, this constituent will be referred to as "coarse

martensite" from this point forward. The coarse martensite is identified by arrows in Figures 1(a), (b), and (c) is a high magnification micrograph of this constituent. Within the constituent, there are particles with different orientation variants, which Fonda and Spanos[23] suggest are cementite. The arrow in Figure 1(c) indicates a light etching, rod-like feature. This is a region of martensite + austenite, and the light etching is an effect of the high nickel concentration of these regions. Using quantitative XRD, the volume fraction of austenite was determined to be 16.9 ± 0.8 vol pct. The average microhardness of the base metal is 335 ± 6 HV.

To understand the composition of the microconstituents of the base metal, LEAP tomography[32–37] was performed. Figure 2(a) shows the 3D-APT reconstruction of the base metal. Fe atoms are shown in blue, Ni atoms are shown in green, and Mo and Cr atoms are shown in red and pink, respectively. The region with the blue hue is Fe-rich and represents the tempered martensite matrix, and the region with the green hue is the Ni-enriched region, which represents the composition of the austenite. Figure 2(b) is a proximity histogram concentration profile[38] across an interface between the Fe- and Ni-enriched regions. This profile shows that Ni and Mn are enriched in the austenite phase, and C, Cr, Mo, and Si are segregated at the interface. Figure 2(c) is the proximity histogram concentration profile across the Fe-rich region and the carbide
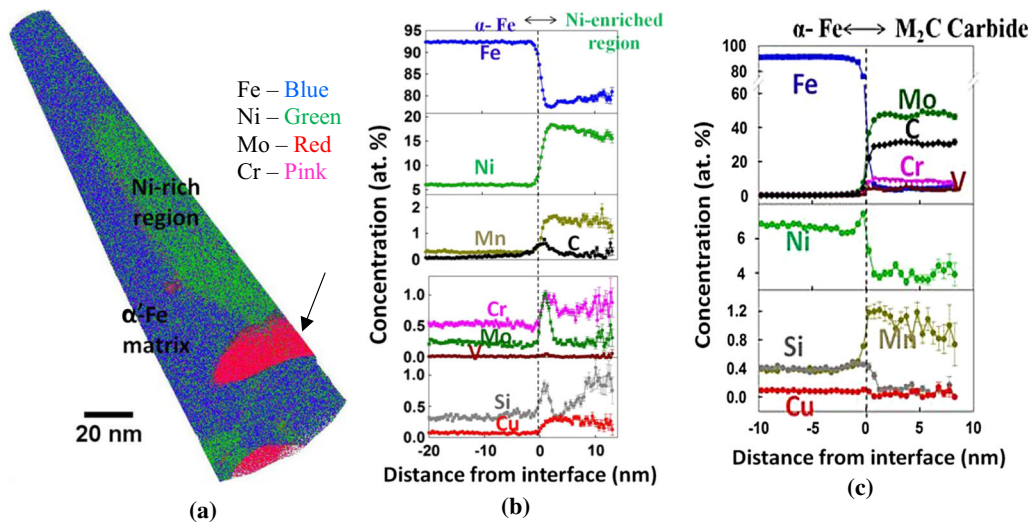
Fig. 2—Local electrode atom probe tomography results of the base metal. (a) 3D-APT reconstruction. Fe atoms are in blue, Ni atoms are in green, Mo and Cr are in red and pink, respectively. (b) Proxigram concentration profiles across the Ni-10 at. pct isoconcentration surface. (c) Proxigram concentration profiles across the (C + Cr + Mo)-10 at. pct isoconcentration surface, delineating the carbide indicated by arrow in (a) (Color figure online).

indicated by an arrow in Figure 2(a). The compositions in at. pct for the tempered martensite and austenite were extracted from the proximity histogram concentration profiles and are provided in Table I. The values for martensite and austenite are from the sample shown in Figure 2(b); two other samples were analyzed for the base metal, but these results have been omitted since the compositions were consistent with the first sample. The composition of the austenite was extracted from the region just beside the martensite/austenite interface because this is representative of the austenite that formed during the tempering portion of the QLT heat treatment.[15] The carbide is enriched in Mo, C, and V, and based on the results of Jain et al.,[15] these are M_2C carbides. Summarizing all the characterization techniques for the base metal, the overall microstructure of 10 wt pct Ni steel is a mixture of tempered martensite with a rod morphology and coarse martensite, 16.9 ± 0.8 vol pct austenite enriched in Ni and Mn, and M_2C carbides.

B. Effect of Heating Rate on Phase Transformations

The first study conducted to understand the overall transformation behavior of 10 wt pct Ni steel was to investigate the effects of heating rate on the transformations and the resultant microstructures. Figure 3 presents the curves of dilation as a function of temperature and their corresponding derivative for the heating rate experiments performed. Figures 3(a) and (c) show the curves for a slow heating rate of 1 °C/s to peak temperatures of 1273 K and 1523 K (1000 °C and 1250 °C), respectively, while Figures 3(b) and (d) show the curves for a rapid heating rate of 1830 °C/s to peak temperatures of 1273 K and 1523 K (1000 °C and 1250 °C), respectively. The critical temperatures Ac_1 (the temperature where austenite begins to form) and Ac_3 (the temperature where the sample has completely

transformed to austenite), are indicated on the figure. Note that, since the starting microstructure contains 16.9 vol pct austenite, the steel does not have a true Ac_1 temperature, as the Ac_1 temperature is defined as the temperature at which a boundary between ferrite and ferrite + austenite would exist on a phase diagram.[39] Since it is known from the base metal XRD that 16.9 vol pct austenite is present at room temperature, there is no such boundary.

The dilatometry plots in Figure 3 show that for the sample heated to a peak temperature of 1273 K (1000 °C), at a 1 °C/s heating rate, the Ac_1 temperature is 857 K (584 °C) and the Ac_3 temperature is 1080 K (807 °C), whereas at an 1830 °C/s heating rate, the Ac_1 temperature is 861 K (588 °C) and no Ac_3 temperature is observed. The evidence in Figure 3(b) that there is no Ac_3 temperature is that the slope of the derivative of the dilation never returns to zero, as the curve continues to be negative even after the large deviation in slope. For the samples heated to a peak temperature of 1523 K (1250 °C), at a 1 °C/s heating rate, the Ac_1 temperature is 843 K (570 °C) and the Ac_3 temperature is 1094 K (821 °C), whereas at an 1830 °C/s heating rate, the Ac_1 temperature is 864 K (591 °C) and the Ac_3 temperature is 1324 K (1051 °C). These results show that the Ac_3 temperature has a strong dependence on heating rate.

Figure 4 shows the dilatometry results for the 1523 K (1250 °C) peak temperature heated at a 1 °C/s over a narrower temperature range than Figure 3. A line tangent to the dilation curve has been imposed. This tangent line shows that the dilation curve contracts from the constant slope at 843 K (570 °C), but the bulk of the transformation does not begin until around 953 K (680 °C). This effect is not typically observed in dilatometry curves of steels. This beginning of the transformation is also manifested by a gentle deviation in the derivative curve from a zero slope, before the large change in slope. Though only described for this
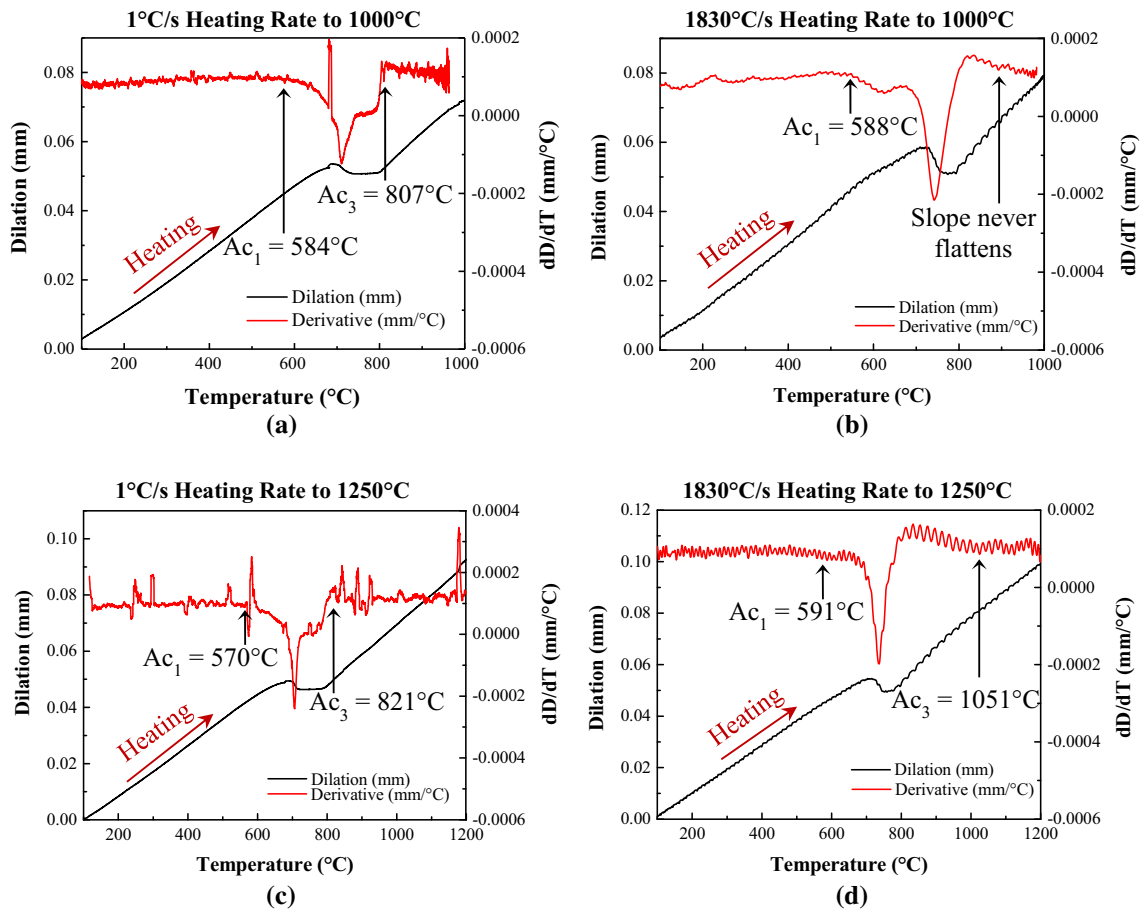
Fig. 3—Dilatometry (black lines) and differentiated dilatometry (red lines) for the heating rate experiments. (*a*) and (*b*) were heated to a peak temperature of 1273 K (1000 °C), while (*c*) and (*d*) were heated to a peak temperature of 1523 K (1250 °C). Austenite start (Ac$_1$) and finish (Ac$_3$) temperatures are labeled accordingly (Color figure online).

sample, this effect was observed in all dilatometry samples. Therefore, the Ac$_1$ temperature for all samples is the beginning of this change in slope.

Figure 5 shows SEM micrographs of the samples used for the heating rate studies. Figures 5(a) and (b) are the samples heated to 1273 K (1000 °C) at 1 and 1830 °C/s, respectively, and Figures 5(c) and (d) are the samples heated to 1523 K (1250 °C) at 1 and 1830 °C/s, respectively. Figures 5(a), (c), and (d) consist completely of as-quenched lath martensite, consistent with their dilatometry plots showing complete transformation to austenite, so on cooling, all of the austenite transformed to martensite. Figure 5(b), however, shows a mixed microstructure of as-quenched lath martensite and rod lath martensite. The as-quenched martensite is indicated by red lines on the micrograph and labeled "FT" for fully transformed. On the dilatometry plot for this sample in Figure 3(b), which was heated to 1273 K (1000 °C) at 1830 °C/s, the slope of the derivative curve never returns to zero by 1273 K (1000 °C), thereby indicating an incomplete transformation to austenite. The microstructure is not fully as-quenched martensite, as some rod martensite never transformed to austenite. Comparing Figures 5(a) and (c), the two samples heated at 1 °C/s to 1273 K and 1523 K (1000 °C and 1250 °C), respectively, Figure 5(c) shows a larger prior austenite
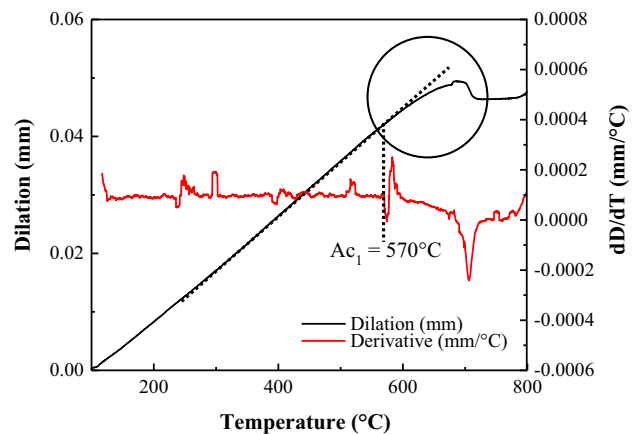

Fig. 4—Dilatometry (black line) and differentiated dilatometry (red line) for the sample heated at 1 °C/s to a peak temperature of 1523 K (1250 °C) magnified to show slight transformation, which is circled (Color figure online).

grain size, since the transformation to austenite was complete at 1094 K (821 °C), so with the increased temperature, there was additional time for the austenite grains to grow. There is an additional difference between the two samples. There are two highlighted regions in Figure 5(a), labeled 1 and 2. Comparing the two areas,
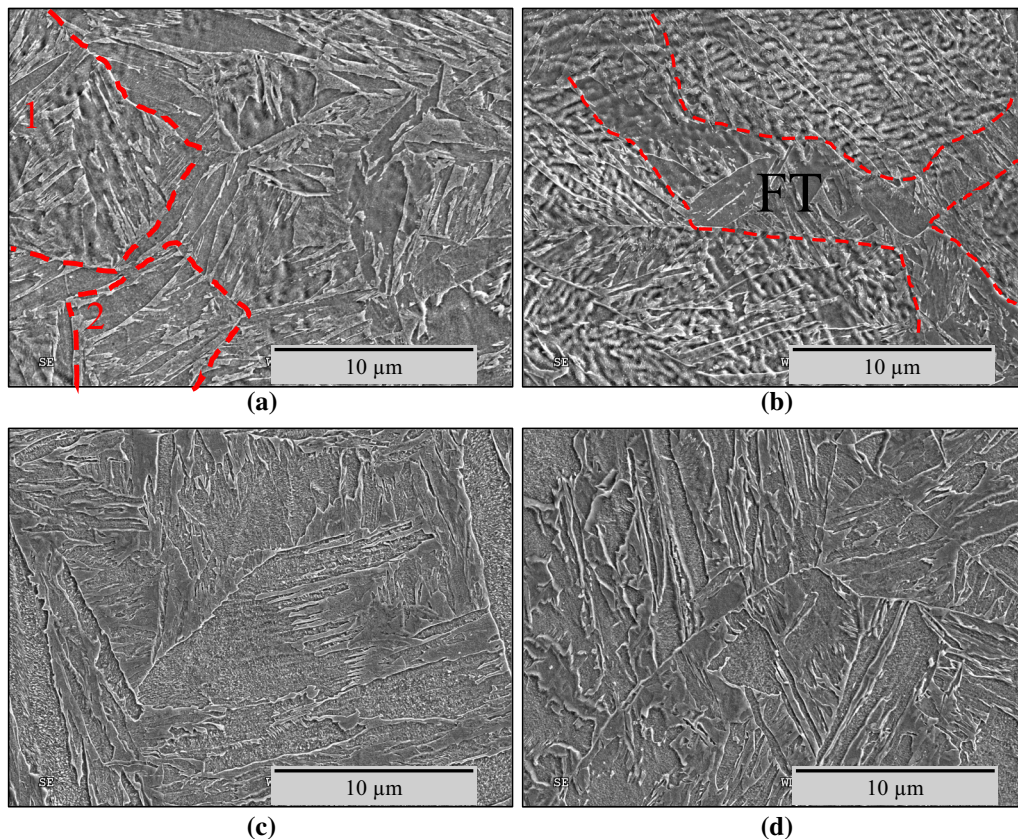
Fig. 5—SEM micrographs of the samples used for the heating rate studies shown in Fig. 2. (*a*) and (*b*) were heated to a peak temperature of 1273 K (1000 °C), while (*c*) and (*d*) were heated to a peak temperature of 1523 K (1250 °C). (a) and (b) were heated at 1 °C/s, while (b) and (d) were heated at 1830 °C/s.

region 1 has dark contrast reminiscent of the rod lath structure whereas region 2 does not. This remnant rod structure would suggest that the sample did not fully transform to austenite during heating, but the dilatometry curves confirm that this sample did completely transform.

To understand the large dependence of Ac_3 temperature on heating rate, isothermal experiments were performed with dilatometry. Two samples were heated at 1000 °C/s to a peak temperature of 1198 K (925 °C) and held for either 5 seconds or 5 minutes. This temperature was chosen because it is above the Ac_3 temperature at a slow heating rate but below the Ac_3 temperature at a fast heating rate, based on the heating rate results in Figure 4. Figure 6 shows the dilation and derivative of dilation as a function of temperature for the heating portion of the sample that was held for 5 seconds and the Ac_1 temperature is 848 K (575 °C); though not shown, the heating portion of the curve for the sample held for 5 minutes is similar in that it exhibits an Ac_1 temperature of 838 K (565 °C). Based on this plot, at this fast heating rate, the sample did not undergo complete austenite transformation. Figure 7 shows plots of dilation as a function of time for these experiments where Figure 7(a) is the 5 seconds hold sample and Figure 7(b) is the 5 minutes hold sample. On both plots, the plateau at the highest dilation is when the sample

was held at 1198 K (925 °C). The inset plots in the figures show these plateau regions over a narrower time range. A review of the plots reveals that the dilation stays relatively constant for the 5 seconds hold sample, whereas the dilation decreases with time for the entire 5 minutes for the other sample. Since during heating, heat is absorbed and the specimen contracts from the phase change,[39] this decreasing dilation indicates that a phase transformation is continuing during the 5 minutes hold. Figures 7(c) and (d) are SEM micrographs of the 5 seconds and 5 minutes hold samples, respectively. The 5 seconds hold microstructure is mixed tempered rod lath martensite and as-quenched lath martensite, enveloped by a red dashed line, indicating only partial transformation to austenite on heating. The 5 minutes hold sample is completely as-quenched martensite, indicating complete transformation to austenite during the heating and hold cycle. This suggests that at a fast heating rate, 5 seconds is not long enough to completely austenitize 10 wt pct Ni steel, but the transformation can complete with additional time.

C. *Effect of Cooling Rate on Phase Transformations*

The second study conducted to understand the overall transformation behavior of 10 wt pct Ni steel was to determine the effect of cooling rate on phase

transformations. Figure 8 shows SEM micrographs for the samples cooled from 1523 K (1250 °C) at the different cooling rates, where Figures 8(a), (b), (c), and (d) are 0.1, 1, 10, and 50 °C/s, respectively. All four cooling rates exhibit a microstructure of as-quenched lath martensite and the coarse martensite constituent. Within the coarse martensite, there is a noticeable
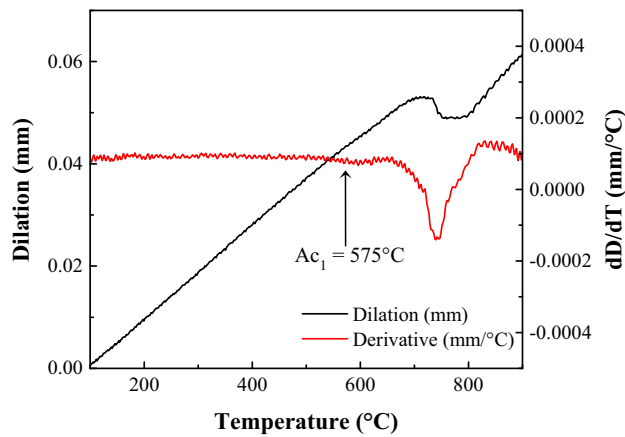

Fig. 6—Dilatometry (black line) and differentiated dilatometry (red line) for the sample heated at 1000 °C/s to a peak temperature of 1198 K (925 °C) (Color figure online).

difference in the appearance of the precipitates. The insets in Figures 8(a) and (d), (a-1) and (d-1), respectively, shows the microstructure of the coarse martensite in the slowest (0.1 °C/s) and fastest (50 °C/s) cooling rates at a higher magnification. For the 0.1 °C/s cooling rate in Figure 8(a-1), the precipitates in the coarse martensite are coarse and few in numbers. By contrast, in the 50 °C/s cooling rate in Figure 8(d-1), the precipitates are fine and present in a larger quantity. The microhardness of the cooling rate samples was also examined. Figure 9 is a plot of microhardness as a function of cooling rate. This plot shows that with increasing cooling rate, the hardness increases. The relatively high hardness of all the samples and the relative consistency within 70 HV confirms that the microstructure of all the cooling rates is martensite. Figure 10 shows example plots of dilation and corresponding derivative curves as a function of temperature for cooling rates of 0.1 °C/s (Figure 10(a)) and 50 °C/s (Figure 10(b)), which were used to determine the transformation temperatures. The M_s temperature is defined as the temperature at which martensite begins to form, and the M_f temperature is when the martensite transformation is complete. These temperatures were determined from the dilation and derivative plots in the same manner as the heating rate experiments. Utilizing the information from the dilatometry plots, microstructure
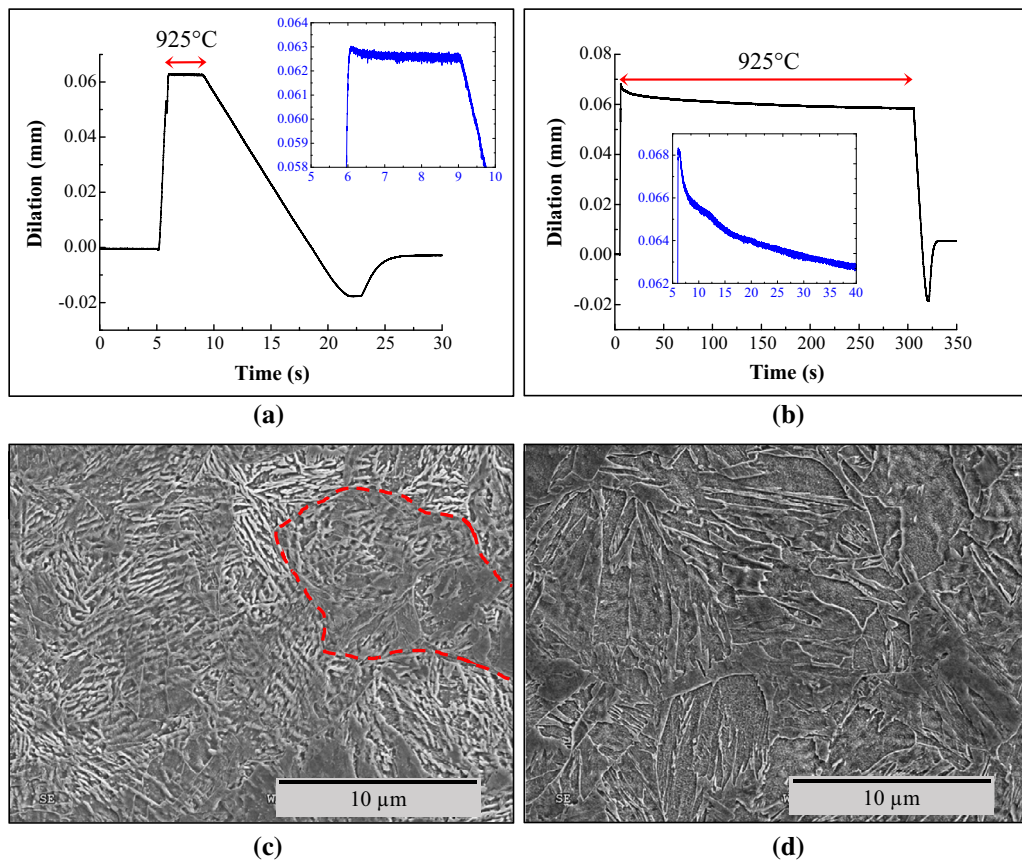

Fig. 7—Dilation as a function of time for the (a) sample heated to 1198 K (925 °C), held for 5 s and (b) the sample heated to 1198 K (925 °C) and isothermally held for 5 min Insets are the same plots magnified to emphasize the dilation contraction in (b). (c) and (d) are SEM micrographs of the samples in (a) and (b), respectively.
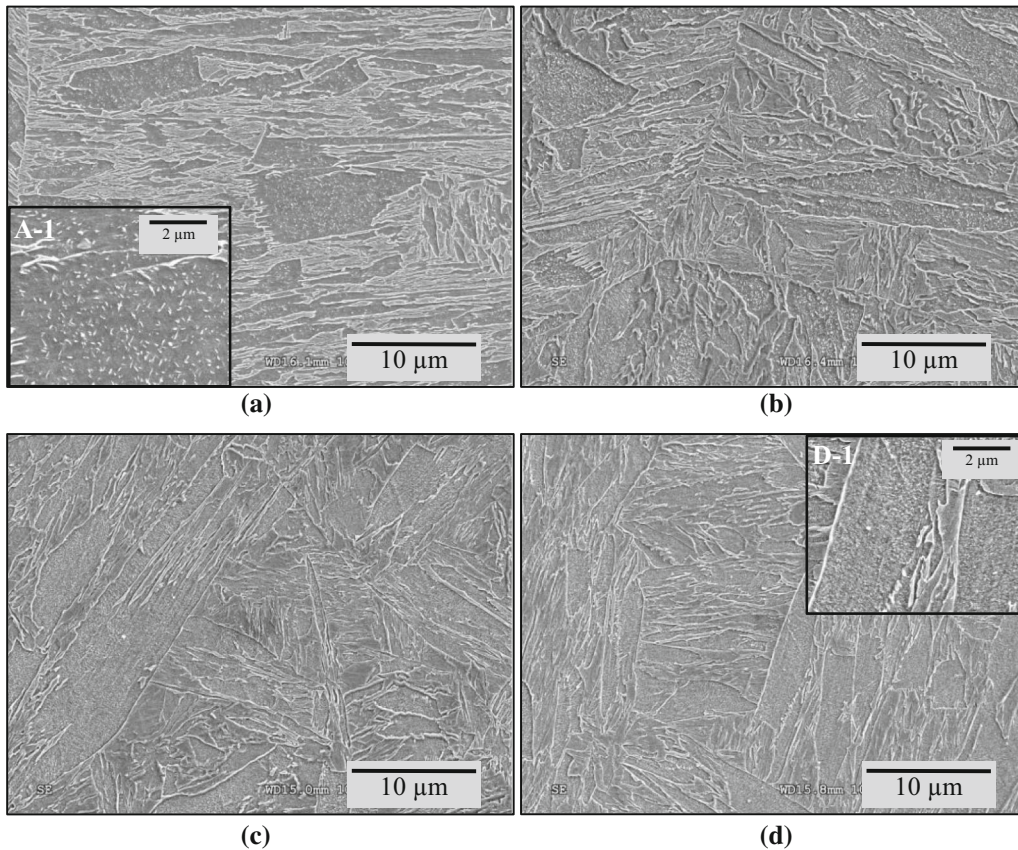
Fig. 8—SEM micrographs of the samples used in determinations of the transformations for the CCT diagram. (*a*) 0.1 °C/s cooling rate, (*b*) 1 °C/s cooling rate, (*c*) 10 °C/s cooling rate, and (*d*) 50 °C/s cooling rate. Insets in (*a*) and (*d*), labeled (*a-1*) and (*b-1*), respectively, are magnified views of the coarse martensite in the samples, emphasizing the size difference of the carbides.
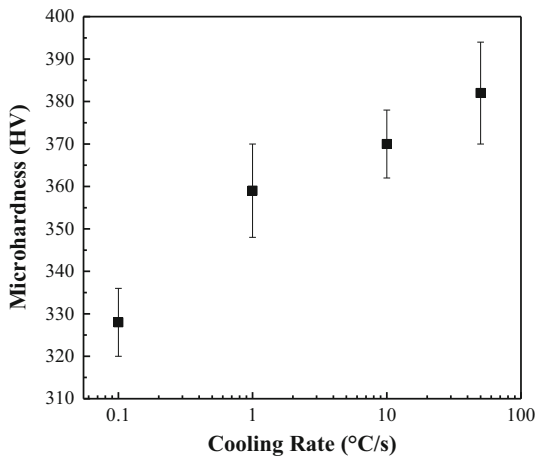

Fig. 9—Microhardness as a function of cooling rate for the four cooling rates used in determination of the CCT diagram.

characterization, and microhardness, a continuous cooling transformation (CCT) curve for 10 wt pct Ni steel was developed and is presented in Figure 11. This diagram shows that the M_s and M_f temperatures are relatively constant across all the cooling rates. The M_s temperature is 685 ± 38 K (412 °C) and the M_f temperature is 466 ± 8 K (193 °C).

D. *Phase Transformations in the HAZ of Gas Tungsten Arc Welds*

Figure 12 shows a microhardness map from across the cross-section of the autogenous, GTAW on QLT 10 wt pct Ni steel weld. Upon inspection using LOM, the location of the fusion line was identified on the map. Figure 13 shows a microhardness trace across the same regions of the weld, labeled as "QLT weld," which was made with a finer indent spacing to identify more subtle details than the microhardness map. The results show that the hardness peaks at some finite distance from the fusion line, and the hardness in any region of the HAZ is never below the base metal hardness. The average hardness of the base metal is 335 ± 6 HV. (It is beyond the scope of this paper to describe the underlying causes of the microhardness trends and this will be discussed in a future paper. The microhardness trends will simply be correlated with the microstructures of the various HAZ regions.)

Based on the microhardness results, select regions were chosen for characterization, and these regions, labeled A through F, are indicated on the microhardness trace in Figure 13. Figure 14 shows LOM micrographs and Figure 15 shows SEM micrographs of the regions on the microhardness trace. In the LOM micrograph in Figure 14(a), region A is similar to the base metal microstructure in Figure 1(a) because light-etching
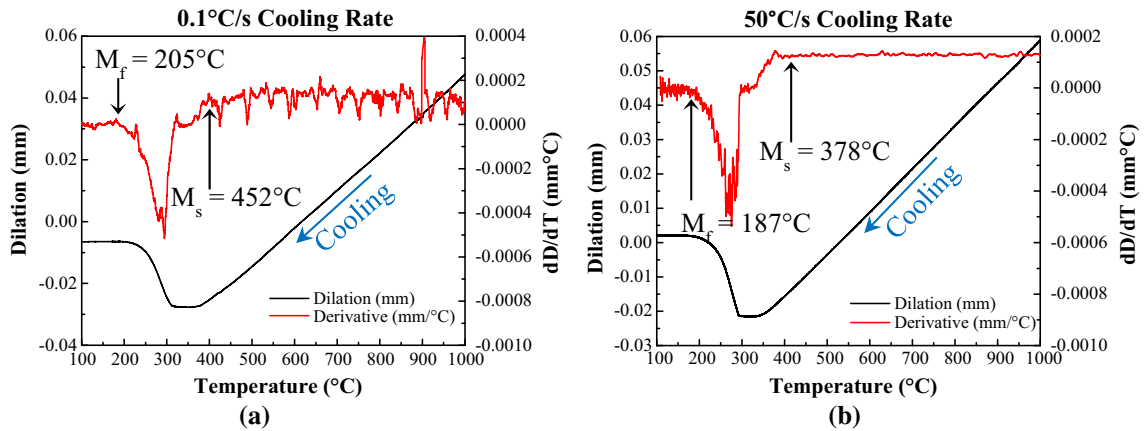
Fig. 10—Example dilatometry (black lines) and differentiated dilatometry (red lines) plots for the (a) 0.1 °C/s and (b) 50 °C/s cooling rate samples used to determine the martensite transformation temperatures in 10 wt pct Ni steel (Color figure online).
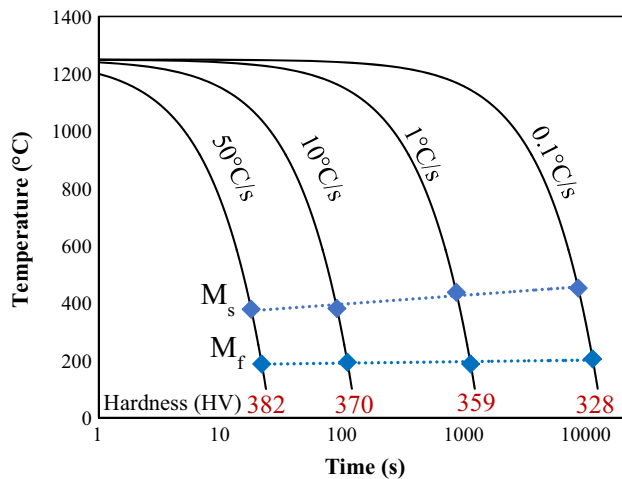

Fig. 11—Continuous cooling transformation diagram for 10 wt pct Ni steel.

regions of coarse martensite are still visible, designated by arrows. Inspection at the SEM level in Figure 15(a) reveals that the microstructure is nearly all rod lath structure, but there are regions identified by arrows that look like they were coarse martensite. There is some internal structure within the coarse martensite that was not present in the base metal sample, which suggests that the coarse martensite may have undergone some transformation or partial transformation during welding. For region B in Figure 14(b), the light-etching regions are blockier than the typical coarse martensite. The SEM micrograph in Figure 15(b) reveals a microstructure that is mostly rod lath structure, but there are also regions that appear to have undergone a transformation, such as the region outlined. There is no coarse martensite present in this region. Region C is the highest hardness region and exhibits an unusual microstructure that consists of a light- and dark-etching constituent shown in Figure 14(c). At the SEM level in Figure 15(c), the microstructure of region C is akin to that of region B, but it contains more of the transformed structure. The reason for the apparent two constituents

in this region will be discussed later. The microstructure of regions D and E is difficult to identify at the LOM level; at the SEM level in Figure 15(d), region D consists of a mixture of transformed and rod lath structure. In this region, the transformed structure has the appearance of as-quenched lath martensite, whereas in regions B and C, the transformed structure is difficult to identify. The rod structure in this region is muddled compared with regions B and C, where the rod laths have well-defined edges. These regions of muddled rod structure are outlined in Figure 15(d), and they are interspersed with the as-quenched lath martensite. Region E in Figure 15(e) almost wholly consists of as-quenched lath martensite, however, there is still residual rod lath structure outlined in the figure. This rod lath structure is even more muddled than region D, and this residual rod structure is commingled with the as-quenched lath martensite, as they appear to lay on top of one another, especially highlighted in the outlined region. Finally, region F, which is the closest to the fusion zone, consists of as-quenched lath martensite and coarse martensite, as evident in Figures 14(f) and 15(f). The coarse martensite is identified by arrows in Figure 15(f).

Two regions of the HAZ were chosen for further analysis using LEAP tomography. Figure 16 shows the LEAP results from region B and Figure 17 shows the LEAP results from region C. Figures 16(a) and 17(a) show the 3D-APT reconstruction of the region. Fe atoms are shown in blue, Ni atoms are shown in green, and Mo and Cr atoms are shown in red and pink, respectively. The region with the blue hue represents the martensite matrix, and the region with the green hue, the Ni-enriched region, represents the austenite. Figures 16(b) and 17(b) are proximity histogram concentration profiles across an interface between the Fe- and Ni-enriched regions. Figure 16(c) is the proximity histogram concentration profile across the Ni-rich region and the carbide indicated by an arrow in Figure 16(a) for region B. No carbides are observed in region C. The compositions for the martensite and austenite were extracted from the proximity histogram concentration profiles and are provided in Table II for both regions.
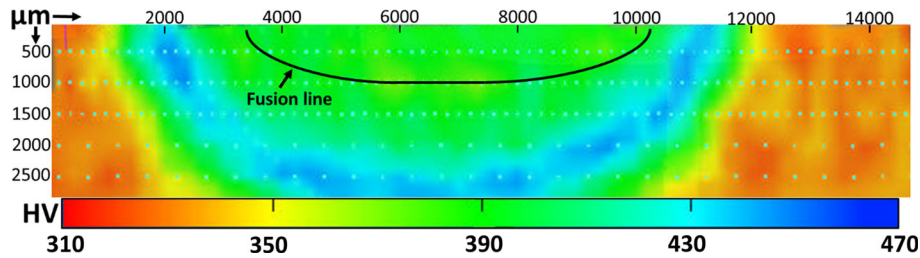
Fig. 12—Microhardness map of the gas tungsten arc weld made on 10 wt pct Ni steel.
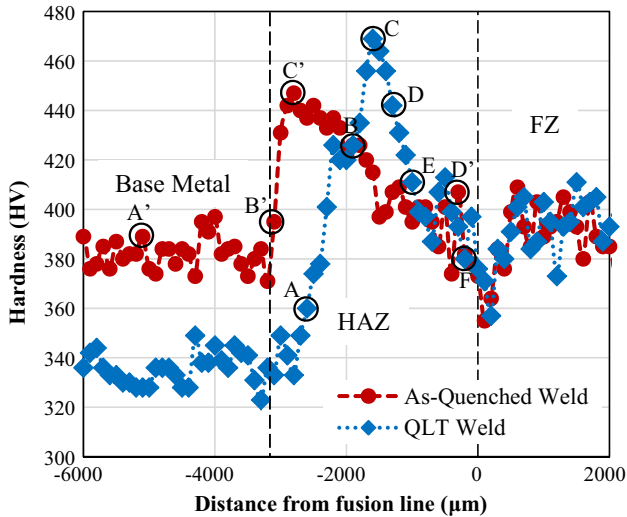

Fig. 13—Microhardness traces across the gas tungsten arc welds that were made on 10 wt pct Ni steel base plate that was QLT heat treated and base plate that was heat treated to form all as-quenched martensite. Circled indents are regions used for analysis.

For each region, a second sample was analyzed and the results are consistent, so they are omitted. Comparing the LEAP results for regions B and C with those of the base metal in Table I, the Ni concentration in the austenite is highest in the base metal and lowest in region C. This decrease in Ni concentration is accompanied by an increase in Ni concentration in martensite in regions B and C. A likely consequence of the lack of carbides in region C is that the carbon concentration in the austenite is higher than region B and the base metal, suggesting that carbides may have dissolved in this region.

The microhardness results for the weld made on the base metal heat treated to produce a microstructure solely consisting of as-quenched martensite (and no austenite), labeled "as-quenched weld," is shown in Figure 13. The microhardness trends for this weld are the same as the "QLT weld" in that the hardness peaks in the HAZ, and the hardness of the HAZ is never below that of the base metal. Four regions were selected for analysis, labeled A′ through D′, and the SEM micrographs of these regions are shown in Figure 18. Figure 18(a′) is the base metal, and the microstructure consists of as-quenched lath martensite. Figure 18(b′) is a two-constituent microstructure with tempered lath martensite and as-quenched lath martensite, an example

of which is outlined. Figure 18(c′), which is the highest hardness region, is fine as-quenched lath martensite, and Figure 18(d′) is coarse as-quenched lath martensite and coarse martensite. The rod lath structure exhibited in the QLT weld is never observed in the as-quenched weld.

IV. DISCUSSION

A. Critical Transformation Temperatures During Heating

The Ac_1 temperature at a slow heating rate of 1 °C/s is 843 K (570 °C) and at a fast heating rate of 1830 °C/s is 864 K (591 °C). As previously described, after the Ac_1 temperature, there is a region of minor transformation before the majority of the transformation, as shown in Figure 4. The majority of the transformation manifests itself as the large contraction in the dilation, whereas the minor transformation is a small contraction in dilation. Two suggestions are provided for interpretation of the initial, small contraction. First, since there is 16.9 vol pct austenite present in the base metal, this small contraction represents growth of the existing austenite. Wei et al.[40] observed the same slight transformation in an Fe-C-Mn-Si alloy with a starting microstructure of as-quenched martensite and small amounts of austenite, and attributed it to the ability of the austenite to grow without a nucleation barrier.

The second suggestion is that martensite, which is compositionally rich in Ni, nucleates austenite at a lower temperature than martensite depleted in Ni. As described by Jain et al.,[15] some of the austenite formed during the L portion of the QLT heat treatment is not stable, so it transforms to martensite during cooling. Since martensitic transformations are displacive and diffusionless, the product martensite has the same composition of the parent austenite,[39] therefore, this fresh martensite is rich in austenite-stabilizing elements. Then during the T treatment, this fresh martensite transforms to austenite and remains stable. However, it is possible that not all of the fresh martensite formed after the L treatment transforms to austenite during the T treatment, so there may be martensite present in the base metal that is compositionally rich in Ni relative to the tempered martensite shown in Table I. Since the LEAP results do not provide any crystallographic information, some portion of the Ni-rich region in the reconstructions could be martensite as opposed to austenite. From the LEAP results of the base metal in
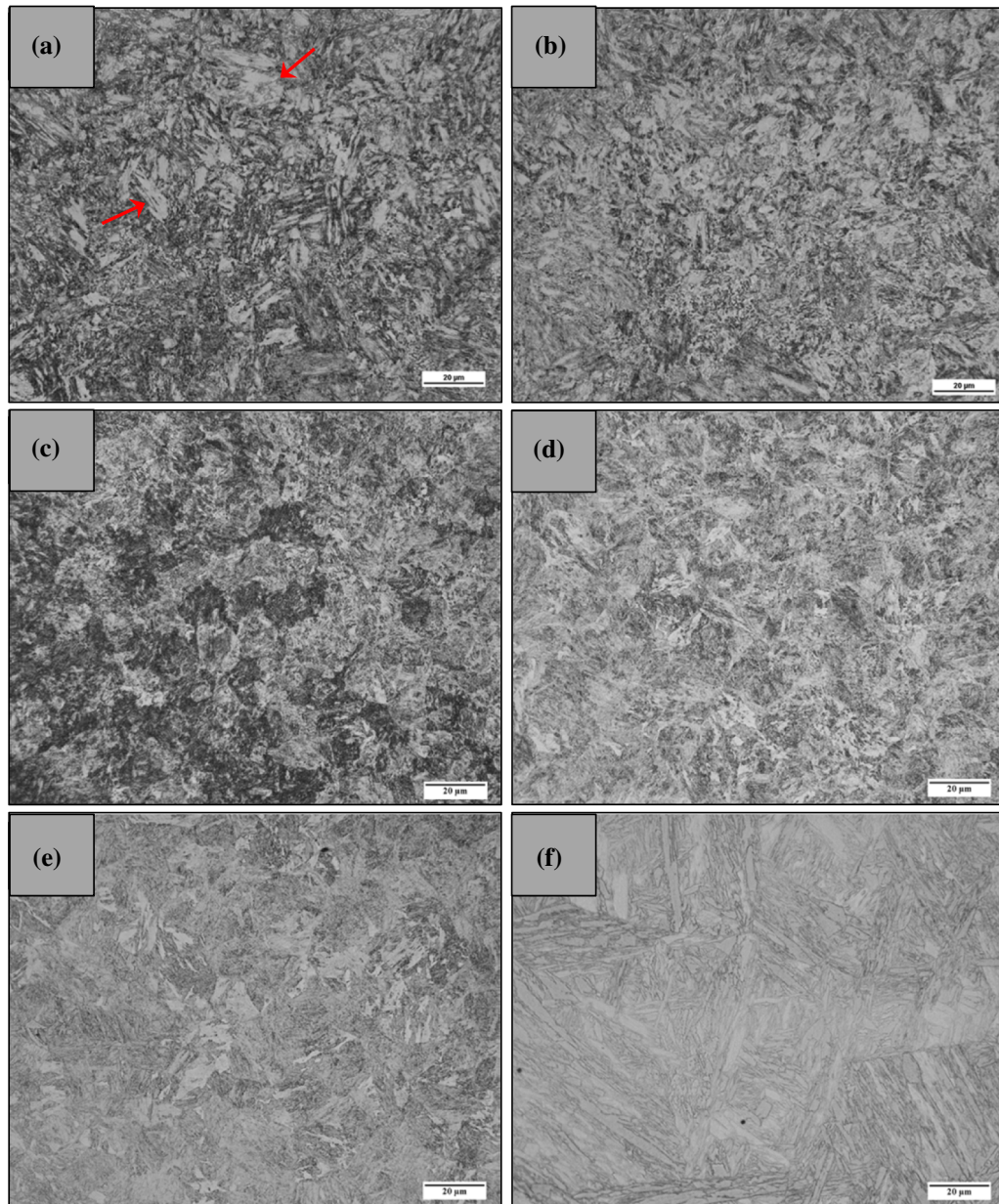
Fig. 14—Light optical micrographs of selected regions of the gas tungsten arc weld made on QLT heat-treated base plate. The regions (*a*), (*b*), (*c*), (*d*), (*e*), and (*f*) correspond to the circled indents on the microhardness trace in Fig. 13.

Figure 2, the tempered martensite contains 6.00 at. pct Ni and the Ni-rich region contains 18.26 at. pct Ni. To observe how austenite formation during heating would be affected by compositionally different as-quenched martensite, Thermo-Calc phase volume fraction plots as a function of temperature were created. Figure 19 shows three different phase fraction plots; Figure 19(a) is the plot using the nominal composition of 10 wt pct Ni steel from Table I, Figure 19(b) is a plot where the "nominal" input composition was the composition of the martensite from the LEAP results in Table I, and Figure 19(c) is a plot where the nominal composition was the composition of the Ni-rich region from the LEAP results in Table I. Figure 19(c) represents the martensite that formed after the L treatment that is

enriched in Ni. Even though the heating rate experiments do not represent equilibrium conditions, the results from Thermo-Calc can still provide valid trends. In all three plots, the major phases are austenite (γ), ferrite (α), M_2C carbides, and γ_2, which is an FCC phase that Thermo-Calc predicts to be compositionally different from γ, in that it is richer in Ni and Fe, but lower in Mn. Martensite is not predicted by Thermo-Calc because it is not an equilibrium phase, so α will be accepted as martensite. The Ac_3 temperature is taken where α phase volume fraction is zero. It is not possible to designate a true Ac_1 temperature, as the phase fraction of austenite is never zero, therefore the Ac_1 temperature is labeled on the plots as "start of transformation." In all three cases, starting from a
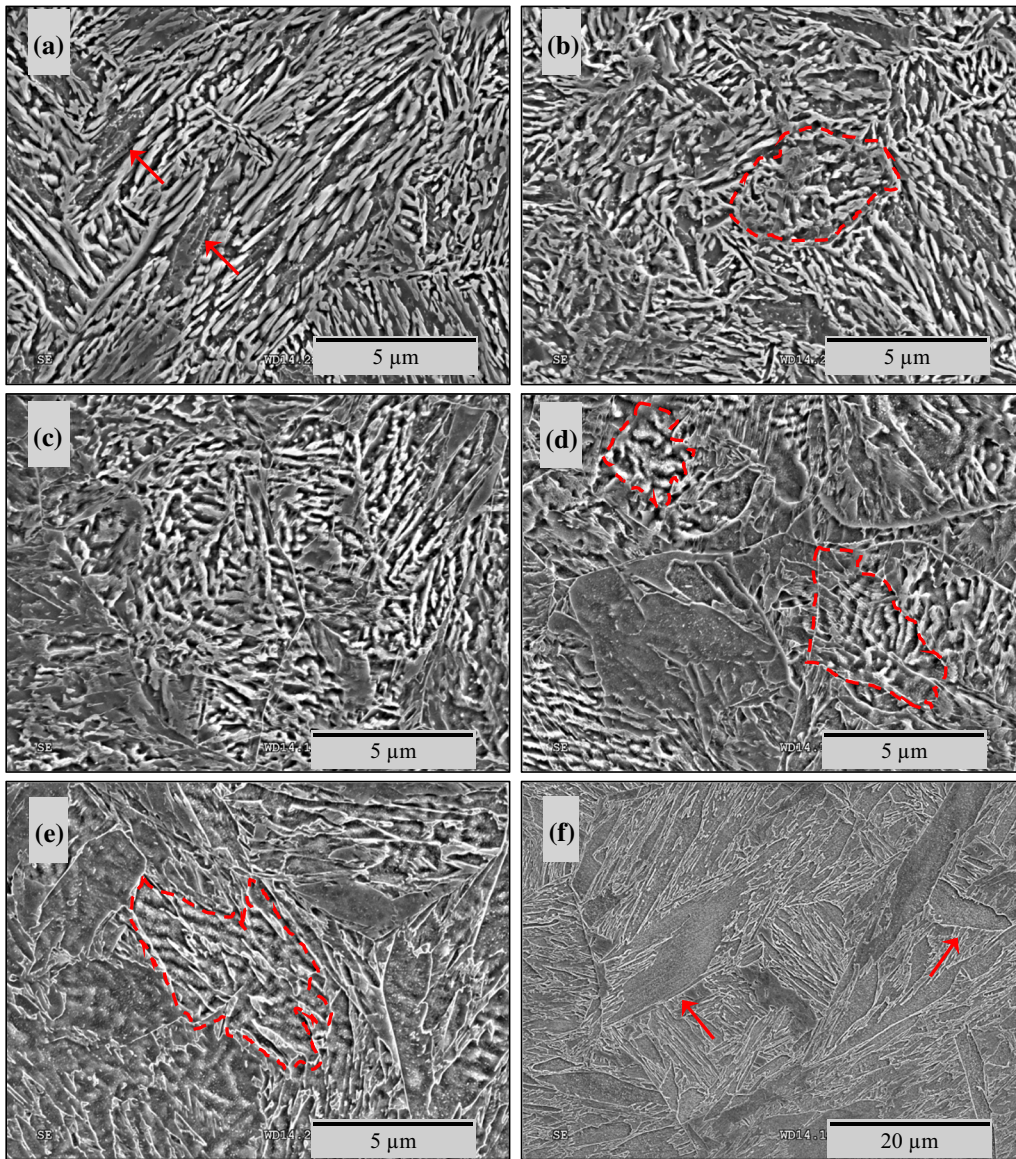
Fig. 15—SEM micrographs of selected regions of the gas tungsten arc weld made on QLT heat-treated base plate. The regions (*a*), (*b*), (*c*), (*d*), (*e*), and (*f*) correspond to the circled indents on the microhardness trace in Fig. 13.

temperature of 473 K (200 °C) and then increasing in temperature, α is at a constant phase fraction until it reaches a temperature at which point it starts to decrease at the expense of γ increasing in phase fraction. Therefore, the start of transformation is taken as the point where α starts to decrease. This point was chosen because this formation of γ on the phase fraction plot would be observed as the contraction in dilation on the dilatometry plot. The Ac_1 and Ac_3 transformation temperatures for the nominal composition are 634 K and 950 K (361 °C and 677 °C), respectively, the temperatures for the tempered martensite composition are 698 K (425 °C) and 999 K (726 °C), and the temperatures for the Ni-rich martensite composition are 553 K and 857 K (280 °C and 584 °C). It is recognized that the phase volume fraction plots can be misleading as the austenite phase is predicted to be stable even when using the composition of martensite that was experimentally

determined. This is a result of how calculations are performed in Thermo-Calc—a nominal composition is provided and assumed to be homogenous across a sample. So even though phases with different compositions are present in the base metal of 10 wt pct Ni steel, to observe how each individual phase varies with temperature, a separate calculation was performed. These results show that the Ni-rich martensite composition has lower transformation temperatures than the tempered martensite composition, which is the majority of the microstructure. Therefore, the Ni-rich martensite will begin the reverse transformation to austenite before the tempered lath martensite. This compositionally different martensite that begins the austenite transformation at a lower temperature results in the slight contraction in the dilatometry results.

The Ac_3 temperature is more dependent on heating rate than the Ac_1 temperature, as the Ac_3 temperature

Fe – Blue
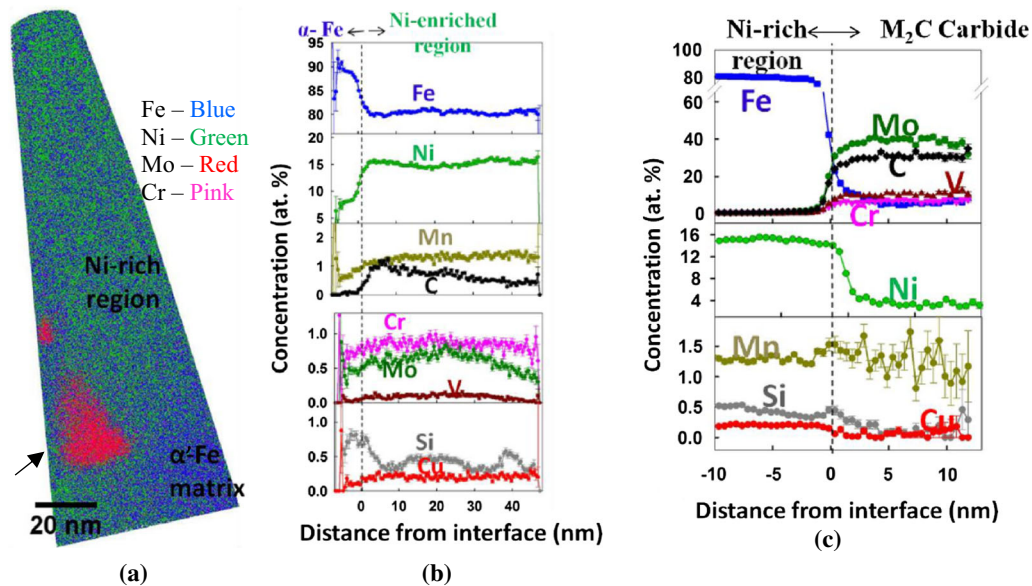Ni – Green
Mo – Red
Cr – Pink

Fig. 16—Local electrode atom probe tomography results for region "B" on the microhardness trace in Fig. 13. (a) 3D-APT reconstruction. Fe atoms are in blue, Ni atoms are in green, Mo and Cr are in red and pink, respectively. (b) Proxigram concentration profiles across the Ni-11 at. pct isoconcentration surface. (c) Proxigram concentration profiles across the (C + Cr + Mo)-10 at. pct isoconcentration surface, delineating the carbide in (a) (Color figure online).
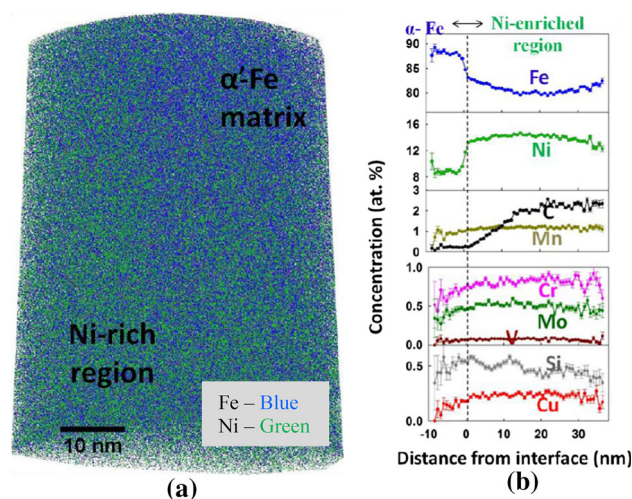

Fig. 17—Local electrode atom probe tomography results for region "C" on the microhardness trace in Fig. 13. (a) 3D-APT reconstruction. Fe atoms are in blue and Ni atoms are in green. (b) Proxigram concentration profiles across the Ni-11 at. pct isoconcentration surface (Color figure online).

varies by ~ 200 K (200 °C) between 1 and 1830 °C/s, whereas the Ac_1 only varies by ~ 20 K (20 °C). It is well known that the reverse transformation of martensite to austenite can proceed *via* a diffusional transformation or shear transformation, which is displacive and diffusionless.[39] The diffusional mechanism in carbon and alloy steels requires interstitial diffusion of carbon as well as substitutional diffusion of austenite-stabilizing elements such as Ni,[41–43] whereas the shear mechanism requires that diffusion be suppressed. For most steels, the diffusional mechanism is dominant at all heating rates, but in higher alloy content steels, the shear mechanism

has been observed.[44–46] Within one system where both mechanisms occur, the shear mechanism typically happens at faster heating rates, whereas the diffusional mechanism happens at slower heating rates. From the LEAP compositions shown in Tables I and II, the concentration of Ni in the Ni-enriched region is lowest in region C, intermediate in region B, and highest in the base metal, whereas in the martensite, the concentration of Ni is highest in region C, intermediate in region B, and lowest in the base metal. This suggests that during heating, the Ni is diffusing across the martensite/austenite interface from the high Ni regions to the martensite. If the reverse transformation were to proceed *via* the diffusional mechanism, the time required for austenite formation would be dependent on the time for Ni to diffuse, since Ni is one of the slowest diffusing elements in steel.[47] With higher heating rates, the time for diffusion decreases, so to compensate, the transformation temperature needs to be higher. The diffusional transformation was experimentally demonstrated with the isothermal dilatometry experiments. The microstructure of the sample held at 1198 K (925 °C) for 5 seconds is mostly rod lath martensite similar to the base metal, whereas the sample held for 5 minutes consists completely of as-quenched lath martensite. The 5 minutes allowed more time for Ni diffusion, therefore the reverse transformation to austenite could proceed *via* diffusion. The isothermal experiments demonstrate that it is possible for the reverse transformation to proceed *via* the diffusional mechanism; however, it does not suggest that the reverse transformation *always* proceeds with the diffusional mechanism. Instead, it is possible that the reverse transformation is a shear transformation, and the Ni diffusion occurs irrespective of the shear mechanism. The Ni will naturally diffuse from areas of high concentration (the original austenite) to areas of low

Table II. Composition of Regions "B" and "C" on the Microhardness Trace in Fig. 13.

	Fe	C	Ni	Mo	V	Cr	Mn	Si	Cu
Martensite (region B)	89.66 ± 0.52	0.07 ± 0.03	7.69 ± 0.46	0.39 ± 0.11	0.04 ± 0.03	0.65 ± 0.14	0.62 ± 0.13	0.64 ± 0.13	0.12 ± 0.06
Martensite (region C)	88.24 ± 0.49	0.33 ± 0.09	8.71 ± 0.43	0.36 ± 0.09	0.05 ± 0.03	0.65 ± 0.12	0.88 ± 0.14	0.47 ± 0.10	0.12 ± 0.05
Ni-rich (region B)	80.05 ± 0.31	0.96 ± 0.07	15.51 ± 7.69	0.57 ± 0.06	0.09 ± 0.02	0.83 ± 0.07	1.13 ± 0.08	0.45 ± 0.05	0.21 ± 0.04
Ni-rich (region C)	80.03 ± 0.26	2.67 ± 0.11	13.78 ± 0.23	0.48 ± 0.04	0.07 ± 0.02	0.83 ± 0.06	1.17 ± 0.07	0.44 ± 0.04	0.23 ± 0.03

The compositions of martensite and austenite was measured using the local atom probe tomography results in Figs. 16 and 17. All results are in at. pct.

concentration (tempered martensite), and this diffusion is enhanced because of the high temperatures experienced during heating.[48]

In summary, the Ac_3 temperature is much higher for faster heating rates than for slower heating rates. It is unknown whether the reverse transformation proceeds *via* a diffusional or shear mechanism, however, isothermal experiments demonstrate that the diffusional mechanism is possible in this alloy system. LEAP results demonstrate that Ni diffuses from original austenite (produced during the QLT treatment) to the lower-Ni martensite regions. This Ni diffusion may be an indication of the reverse transformation proceeding *via* the diffusional mechanism or it may just progress alongside the shear transformation, since it is enhanced by the concentration gradient and elevated temperatures. Nevertheless, even though the mechanism of reverse transformation is uncertain, these results are significant for welding because the large temperature range between the Ac_1 and Ac_3 temperatures at high heating rates will produce a large intercritical (ICHAZ) region. This is an important consideration when interpreting the HAZ microstructures. These results are also significant because they demonstrate the sluggish Ni diffusion, the importance of which will be described below.

As mentioned, despite the dilatometry results for the 1 °C/s heating rate sample to a peak temperature of 1273 K (1000 °C) showing complete austenite transformation, there is still evidence of rod lath structure as indicated in Figure 5(a). It is suggested that this residual structure is a result of remnant compositional differences. As was described for the base metal, the light etching, rod features are regions of martensite + austenite, and the light etching is an effect of the high Ni concentration of these regions. The proxigram concentration profile for the base metal LEAP sample in Figure 2(b) shows that the Ni concentration in the austenite is highest just beside the martensite/austenite interface and then decreases in the austenite with increasing distance from the interface. The proxigram concentration profile for region C in Figure 17(b) shows that Ni concentration beside the interface is much lower than in the base metal, but the Ni concentration further from the interface is still relatively constant. This suggests that the Ni diffusing across the interface during heating is coming from the regions closest to the interface, while the Ni at the center of the austenite is relatively stagnant. As the reverse transformation proceeds, new austenite is formed beside the original austenite/martensite interface. Therefore, the Ni trapped in the center of the original austenite has a larger distance to travel, it must travel through austenite, and Ni diffusion is even slower in austenite than in ferrite.[47] Thus, for the Ni to totally homogenize, even more time is required. The residual rod lath microstructure is still visible in the 1 °C/s heating rate sample to a peak temperature of 1273 K (1000 °C), despite having undergone the full austenite transformation because the Ni is still not fully homogenized. Therefore, the residual rod lath microstructure is still observed because of the remnant compositional differences. This makes it difficult to distinguish microstructures in the HAZ of 10 wt
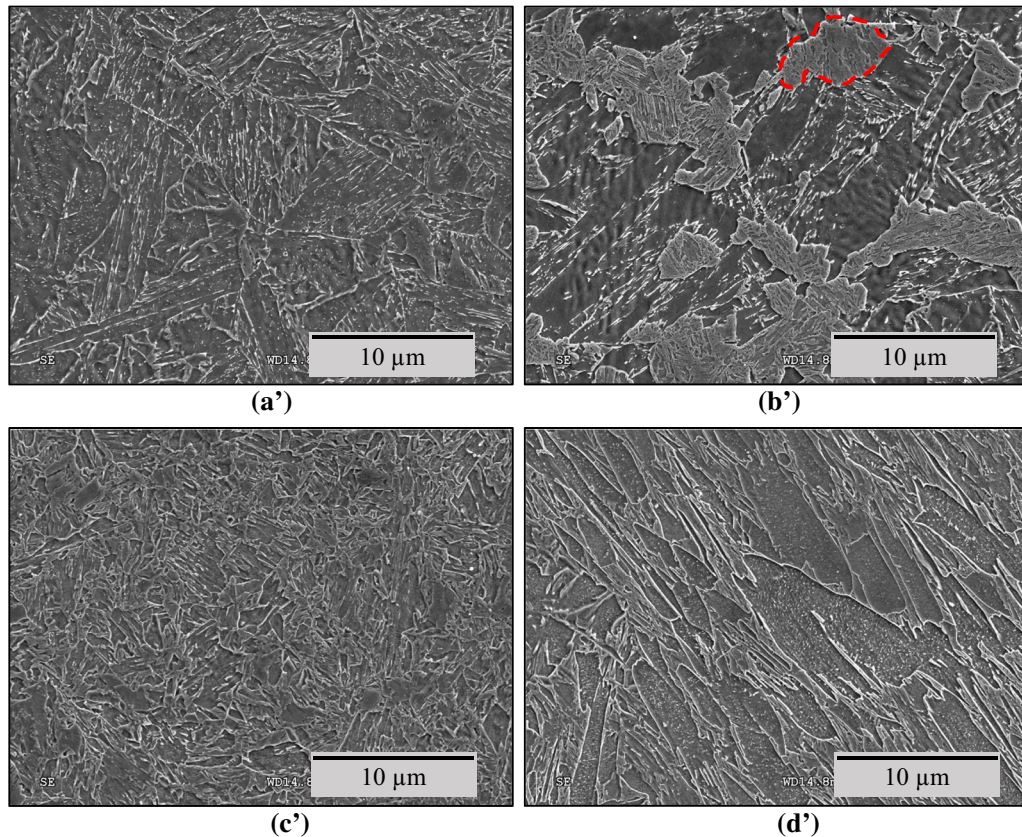
Fig. 18—SEM micrographs of selected regions of the gas tungsten arc weld made on the as-quenched martensite base plate. The regions (a'), (b'), (c'), and (d') correspond to the circled indents on the microhardness trace in Fig. 13.

pct Ni steel that were heated to above the Ac_3 temperature from those that were heated to intermediate temperatures between Ac_1 and Ac_3.

B. *Cooling Rate Effects on Phase Transformations*

All of the microstructures of the cooling rate samples consist of as-quenched lath martensite and coarse martensite. No rod lath martensite is observed because the sample was held at 1523 K (1250 °C) for 5 minutes before cooling, which allowed the Ni to homogenize, thereby eliminating austenite in the microstructure. Consistent with what was found by Fonda and Spanos,[23] the size, shape, and presence of the coarse martensite is independent of cooling rate. Therefore, the presence of coarse martensite in 10 wt pct Ni steel is not dependent on cooling rate, but rather is dependent on the peak temperature and heating rate during reheating of the base metal. The heating rate samples that did not undergo a full austenite transformation, such as the 1830 °C/s sample heated to 1273 K (1000 °C), does not show any coarse martensite. Additionally, for coarse martensite to form, the peak temperature needs to be sufficiently above the Ac_3 temperature, since the sample heated at 1 °C/s to 1273 K (1000 °C) did not show any coarse martensite, but the sample heated at 1 °C/s to 1523 K (1250 °C) did show coarse martensite. This is consistent with the mechanism of coarse martensite

formation proposed by Bhadeshia *et al.*[29] and Fonda and Spanos[23] that large austenite grain sizes are necessary for the constituent to form. Therefore, coarse martensite is only present in 10 wt pct Ni steel that has experienced a heating and cooling thermal cycle if the sample is heated to a peak temperature sufficiently above Ac_3 to where relatively large austenite grains are produced. The only difference in the coarse martensite microstructure between the different cooling rate samples is the size and number of cementite precipitates. The slowest cooling rate has few large precipitates, whereas the fastest cooling rate has many fine precipitates. This suggests that the precipitates coarsened in the slow cooling rate since there was more time for diffusion during cooling. Applying this to the coarse martensite in the base metal in Figure 1(c), the relatively small volume fraction of precipitates present suggests that the coarse martensite forms during the Q treatment, and then the precipitates coarsened during the L and T portions of the QLT heat treatment.

The microhardness increases with increasing cooling rate. Comparing the microstructures of the samples, the fastest cooling rate has the smallest prior austenite grain size whereas the slowest cooling rate has the largest prior austenite grain size, therefore the prior austenite grain size decreases with increasing cooling rate. This is because at the slower cooling rates, there is more time for the austenite grains to grow before the martensite
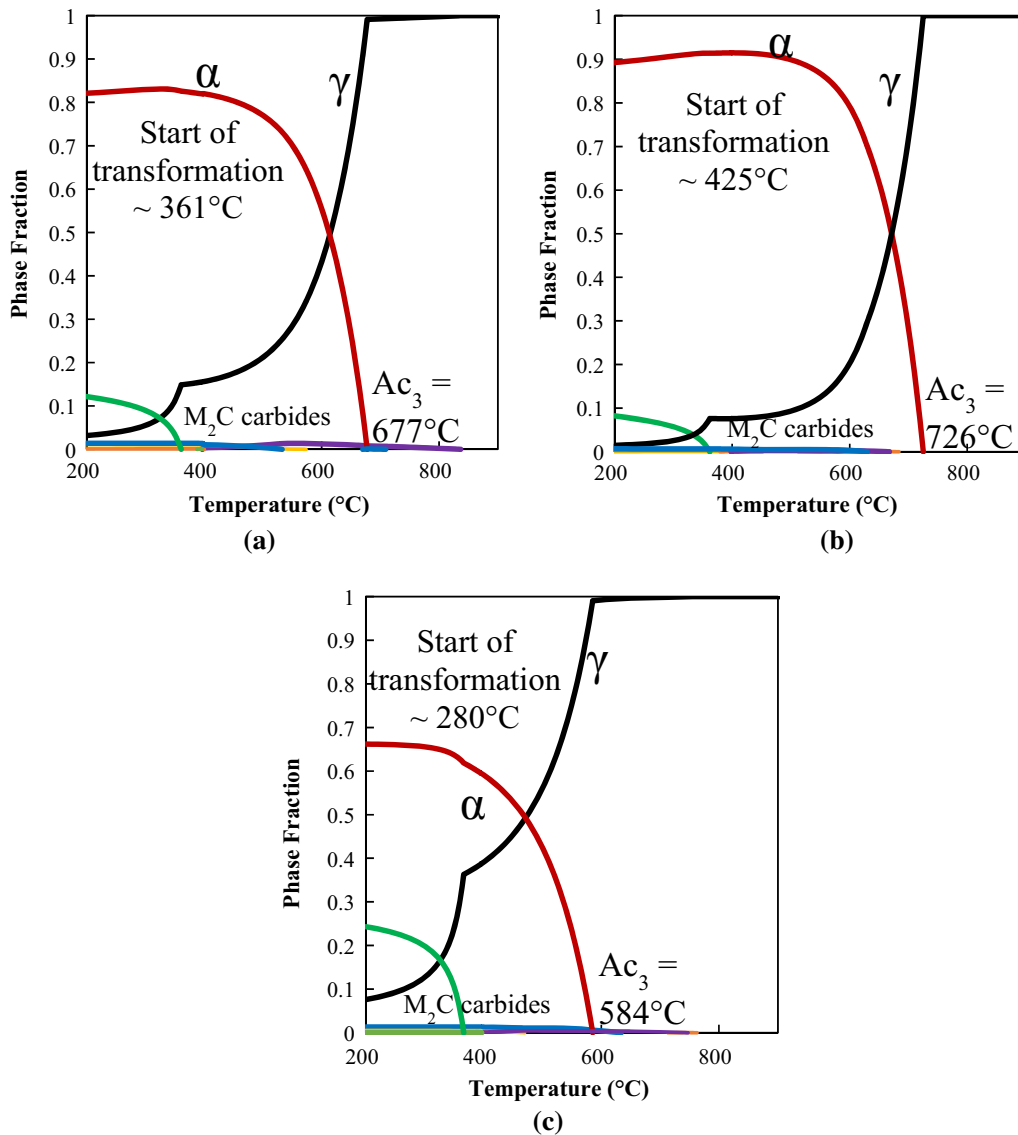
Fig. 19—Thermo-Calc calculations showing the phase volume fraction as a function of temperature in 10 wt pct Ni steel. (*a*) Plot calculated using the nominal composition of the alloy. (*b*) Plot calculated using the composition of the martensite determined *via* LEAP tomography. (*c*) Plot calculated using the composition of the austenite determined *via* LEAP tomography.

transformation takes place. Since the martensite transformation is displacive and thereby diffusionless, the size of the parent austenite grain directly determines the size of the prior austenite grain boundaries. Therefore, the difference in hardness could be a result of the decreasing prior austenite grain size, as the strength of lath martensite is inversely related to the prior austenite grain size.[39] Another option for the hardness differences is the size and dispersion of the cementite within the coarse martensite. The hardest sample is the 50 °C/s, which contains the finest and most widely dispersed carbides in the coarse martensite. On the other hand, the 0.1 °C/s sample is the softest and the carbides are larger and there are fewer. In a similar cooling rate study of 9 wt pct Ni steel,[23] the microhardness results across the different cooling rates was more constant than the results presented here for 10 wt pct Ni steel. This could

suggest that 10 wt pct Ni steel is more sensitive to the prior austenite grain size, the cementite size and distribution within the coarse martensite, or there may be some other microstructural factor in 10 wt pct Ni steel such as M_2C carbides not present in 9 wt pct Ni steel that could be causing this difference.

The CCT diagram for 10 wt pct Ni steel shows that the M_s temperature is 685 ± 38 K (412 °C) and the M_f temperature is 466 ± 8 K (193 °C). It is useful to compare the M_s and M_f temperatures to predicted temperatures determined from empirical relationships, however, none of the relationships were developed for such a high nickel content, so technically 10 wt pct Ni steel is outside of the allowed compositional range. Using the formulas developed by Andrews,[49] the predicted M_s using the linear relationship is 560 K (287 °C), and the predicted M_s using the product

relationship[29] is 565 K (292 °C). The predicted B_s temperature using the empirical relationship from Steven and Haynes[50] is 489 K (216 °C), and since the predicted B_s temperature is below both predicted M_s temperatures, this confirms that the expected microstructure is martensite. The large difference in the predicted temperatures and the actual temperatures is most likely a result of the Ni content. This CCT diagram is significant because it shows that martensite will form over a very wide range of cooling rates, which reflects a very high hardenability of 10 wt pct Ni steel. This is identical to what was reported for a similar 9 wt pct Ni steel.[23]

C. Implications of Heating and Cooling Rate Effects in 10 Wt Pct Ni Steel Welds

A summary of the microstructure evolution throughout the HAZ is provided here. The base metal consists of rod lath martensite and coarse martensite. Within the HAZ closest to the base metal, the appearance of the coarse martensite is different as some internal structure within the coarse martensite is seen in region A. The higher hardness of region A compared to the base metal suggests that some transformation on heating has occurred with as-quenched martensite forming on cooling. With further distance from the unaffected base metal, the coarse martensite disappears. The disappearance of the coarse martensite is coincident with larger regions that appear to have transformed, as observed in region B. At the highest hardness region, the microstructure is a mixture of as-quenched lath martensite and rod lath martensite. With decreasing distance to the fusion line, the fraction of as-quenched lath martensite increases while the fraction of rod lath structure decreases, and the rod lath structure becomes increasingly muddled, until the rod structure is completely replaced by as-quenched lath martensite, which occurs beside the fusion zone. The microstructure next to the fusion zone is a mixture of as-quenched lath martensite and coarse martensite.

Typically, the regions of the HAZ would be identified according to standard HAZ terminology for steel welds that include the sub-critical (SCHAZ), ICHAZ, fine grain (FGHAZ), and coarse grain regions (CGHAZ),[4] and these regions are quite easy to identify in carbon and low alloy steels.[51] However, the HAZ microstructures in 10 pct Ni steel are slightly more complex due to the sluggish transformation kinetics, so despite the regions being present, only some of them can be distinguished purely by microstructure. Region F is representative of the CGHAZ. This region experienced the highest peak temperatures and fastest heating rate of the regions surveyed,[4] and the microstructure consists of as-quenched martensite and coarse martensite. This microstructure is akin to the microstructure of the heating rate sample that was heated at 1830 °C/s to 1523 K (1250 °C). Aside from the base metal, this is the only region of the weld that contains coarse martensite. The formation of coarse martensite requires the peak temperature experienced during welding to be well above the Ac_3 temperature where relatively large austenite grains are produced,[29] therefore this is the only region of the HAZ where coarse martensite would be expected. It is unclear whether region E is the FGHAZ or the ICHAZ; the remnant rod structure visible in the 1 °C/s heating rate sample to 1273 K (1000 °C) in Figure 5(a) that completely transformed to austenite suggests that without dilatometry data, the boundary between the ICHAZ and FGHAZ regions cannot be distinguished. Since the CCT diagram shows that 10 wt pct Ni steel easily forms martensite at a range of cooling rates, the ICHAZ should consist of as-quenched martensite and tempered martensite. However, the remnant rod lath structure does not allow for easy determination of which regions of the microstructure transformed and which ones tempered. Based on the distance from the fusion line and the two-constituent microstructure of as-quenched lath martensite and rod lath martensite, it is suggested that region D is part of the ICHAZ. Additionally, the microstructure of region D is similar to the heating rate sample that was heated at 1830 °C/s to 1273 K (1000 °C). Since that heating rate sample was heated to a peak temperature between the Ac_1 and Ac_3 temperature, the microstructure is representative of the ICHAZ. Therefore, since region D has a similar microstructure, it is most likely within the ICHAZ. To identify the ICHAZ from the SCHAZ, a Gleeble HAZ simulation for a peak temperature of 823 K (550 °C) was performed. This peak temperature was chosen because it is below the Ac_1 temperature for 10 wt pct Ni steel, therefore, this simulation is characteristic of the SCHAZ region. Comparing the hardness of the base metal and the simulated SCHAZ, the hardness of the base metal is 335 ± 6 HV and the hardness of the simulated SCHAZ is 331 ± 5 HV. This shows that there is no statistical difference in the hardness of the base metal or the SCHAZ. Since the hardness of region A is 360 HV, which is harder than the base metal, this suggests that region A is the beginning of the ICHAZ, and the regions indicated by arrows in Figure 15(a) are the regions that transformed to austenite during welding. Therefore, regions A through D are part of the ICHAZ. The main difference between the four regions is the extent of the remnant rod lath structure remaining, with region D containing the least amount and region A containing the greatest amount. This inability to distinguish HAZ regions in 10 wt pct Ni steel has not previously been addressed by 9 wt pct Ni steel HAZ studies. This is because the HAZ studies either focused on 9 wt pct Ni steel that had not underwent a QLT treatment[52] or it was QLT base metal but the characterization dealt only with mechanical properties of the HAZ.[8–10,14] Additional Gleeble HAZ simulations with carefully controlled heating and cooling rates and peak temperatures are in progress to conclusively identify the different regions of the HAZ and will be reported in future work.

It is suggested that the muddled rod morphology is a result of the Ni diffusion. The LEAP results for regions B and C show that Ni diffuses across the austenite/martensite interface from the original austenite to the martensite. The rod structure in regions A through C still has well-defined boundaries because there is a short
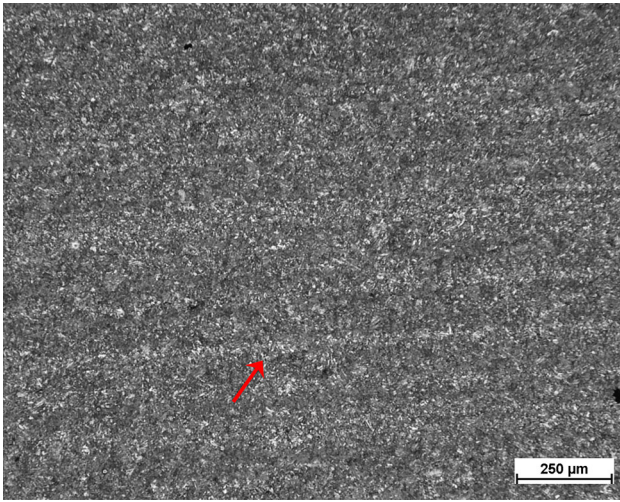
Fig. 20—Light optical micrograph of the base metal of 10 wt pct Ni steel. Arrow indicates light-etching band.

time for the Ni to diffuse. With increasing distance from the base metal, the regions are subjected to higher peak temperatures and increased time at elevated temperatures,[4] so Ni diffusion is more extensive. Regions D and E are further from the base metal, so their rod structure is more muddled because more Ni has diffused across the martensite/austenite interface. No rod structure is observed in the CGHAZ, likely because the Ni is homogenously distributed within the sample. Therefore, the rod structure in the HAZ becoming increasingly more muddled with increased distance from the base metal is consistent with the Ni diffusion.

The LOM micrograph for region C in Figure 14(c) suggests this is a two-constituent region. Upon closer inspection with SEM, both regions primarily consist of rod lath martensite. However, the rod structure in the light-etching regions is more muddled than the rod structure in the dark-etching regions. Figure 20 is a low-magnification LOM micrograph of the base metal that shows the presence of banding. It is suggested that the bands contain different amounts of austenite, with the darker bands containing more austenite than the lighter bands.[53] Therefore, during heating, the light and dark-etching constituents in region C reached different points in the reverse austenite transformation, since the Ni in the austenite drives the transformation. The light-etching regions are further along in the transformation since they have the muddled rod morphology, which is characteristic of the HAZ regions closer to the fusion zone.

Comparing the as-quenched weld to the QLT weld that has been discussed, the rod lath martensite is never observed. The base metal is all as-quenched lath martensite, there is a region of as-quenched lath martensite and tempered martensite, and closest to the fusion line, the microstructure is as-quenched lath martensite and coarse martensite. It is quite easy to identify the different regions of the HAZ; region D′ is the CGHAZ, region C′ is the FGHAZ, and region B′ is the ICHAZ, identified by its two-constituent

microstructure of as-quenched martensite and tempered martensite. As was described for the base metal, the rod structure consists of martensite and austenite, and it etches lightly because of the high Ni content. By heat treating the base metal at 1173 K (900 °C) for 1 hour, there has been time for the Ni to become homogenously distributed throughout the sample, thereby eliminating the austenite. However, in the ICHAZ in Figure 18(b′) remnant segregation is observed in the tempered martensite regions, which suggests that at 1173 K (900 °C), 1 hour is not long enough to completely homogenize the Ni. Nevertheless, this experiment confirms that the rod structure is a result of the 16.9 vol pct austenite in the base metal, and the muddled rod structure in the HAZ is from the diffusion of Ni. There is no microstructural difference observed between CGHAZ in the two welds, which confirms that in the QLT weld, the Ni is homogenously distributed at this point in the HAZ. Therefore, the unique microstructures observed in the HAZ of 10 wt pct Ni steel is a result of the extremely segregated Ni brought on by the three-step QLT heat treatment of the base metal.

V. CONCLUSIONS

The overall transformation behavior of 10 wt pct Ni steel was assessed by studying the effects of heating rate and cooling rate on the phase transformations and microstructure. The results of the cooling rate studies were used to construct a CCT diagram for 10 wt pct Ni steel. The results of the heating rate and cooling rate experiments were applied to a single pass, GTAW, for which the microstructure was characterized. The following conclusions can be drawn:

(1) The overall microstructure of 10 wt pct Ni steel is a mixture of tempered lath martensite with a rod morphology, coarse martensite, 16.9 ± 0.8 vol pct austenite enriched in Ni, and M_2C carbides.
(2) The Ac_1 and Ac_3 temperatures of the steel are dependent on heating rate. The Ac_1 and Ac_3 temperatures when the sample is heated at 1 °C/s are 843 K and 1094 K (570 °C and 821 °C), respectively, and the Ac_1 and Ac_3 temperatures when the sample is heated at 1830 °C/s are 864 K and 1324 K (591 °C and 1051 °C), respectively.
(3) The dilatometry results for the heating rate experiments demonstrate a region of minor transformation after the Ac_1 temperature before the majority of the microstructure transforms. It is suggested that a small portion of the microstructure could transform to austenite on heating before the rest because existing austenite would grow without requiring nucleation, or Ni-enriched martensite left over from the base metal QLT heat treatment would nucleate austenite at a lower temperature than the majority of the martensite, which is relatively low in Ni.
(4) There is a large dependence on heating rate for the Ac_3 temperature. It is unknown whether the reverse transformation of martensite to austenite

proceeds *via* a diffusional or shear mechanism, but nonetheless the results are significant for welding because the large temperature range between the Ac_1 and Ac_3 temperatures at high heating rates will produce a large ICHAZ region.

(5) The CCT diagram shows that martensite will form over a very wide range of cooling rates, which reflects a very high hardenability of 10 wt pct Ni steel. The M_s temperature is 685 ± 38 K (412 °C) and the M_f temperature is 466 ± 8 K (193 °C).

(6) The microstructure evolution through the HAZ of the single pass, autogenous, GTAW shows that with increasing peak temperature, the rod lath martensite gradually becomes replaced by as-quenched lath martensite, and the rod lath martensite becomes increasingly muddled. The rod structure becomes muddled because of the nickel diffusing out of the original austenite into the martensite during heating. This unique structure is not observed in the single pass autogenous GTAW of the as-quenched 10 wt pct Ni steel, which confirms that the rod morphology is a direct result of the extremely segregated Ni in the austenite brought on by the three-step QLT heat treatment of the base metal.

REFERENCES

1. X.J. Zhang: *Mater. Sci. Technol.*, 2012, vol. 28, pp. 818–22.
2. D. Isheim, A.H. Hunter, X.J. Zhang, and D.N. Seidman: *Metall. Mater. Trans. A*, 2013, vol. 44A, pp. 3046–59.
3. V.F. Zackay, V.F. Parker, E.R. Fahr, and R. Busch: *Trans. Am. Soc. Met.*, 1967, vol. 60, pp. 252–59.
4. H.K.D.H. Bhadeshia and R.W.K. Honeycombe: *Steels: Microstructure and Properties*, 3rd ed., Butterworth-Heinemann, Oxford, 2006, pp. 71–73, 223–26, 298–306.
5. W.W. Gerberich, G. Thomas, E.R. Parker, and V.F. Zackay: *Proc. 2nd Int. Conf. Strength Met. Alloys*, August 30–September 4, 1970, American Society for Metals, Materials Park, OH, 1970, pp. 894–99.
6. J.I. Kim, C.K. Syn, and J.W. Morris: *Metall. Trans. A*, 1983, vol. 14A, pp. 93–103.
7. W.Y. Choo, S.W. Lee, and J.Y. Yoo: *38th Mech. Work. Steel Process. Conf. Proc.*, vol. XXXIV, Cleveland, Ohio, October 13–16, 1996, Iron and Steel Society, Warrendale, PA, 1997, pp. 483–91.
8. J. Jang, Y. Yang, W. Kim, and D. Kwon: *Advances in Cryogenic Engineering Materials*, Springer, New York, 1998, vol. 44, pp. 41–48.
9. J.I. Jang, B.W. Lee, J.B. Ju, D. Kwon, and W.S. Kim: *Metall. Mater. Trans. A*, 2002, vol. 33A, pp. 2615–22.
10. J.I. Jang, J.B. Ju, B.W. Lee, D. Kwon, and W.S. Kim: *Mater. Sci. Eng. A*, 2003, vol. 340A, pp. 68–79.
11. X.Q. Zhao, T. Pan, Q.F. Wang, H. Su, C.F. Yang, Q.X. Yang, and Y.Q. Zhang: *J. Iron Steel Res. Int.*, 2007, vol. 14, pp. 240–44.
12. S.J. Wu, G.J. Sun, Q.S. Ma, Q.Y. Shen, and L. Xu: *J. Mater. Process. Technol.*, 2013, vol. 213, pp. 120–28.
13. Y. Yang, Q. Cai, D. Tang, and H. Wu: *Int. J. Miner. Metall. Mater.*, 2010, vol. 14, pp. 587–95.
14. J.I. Jang, J.S. Lee, J.B. Ju, B.W. Lee, D. Kwon, and W.S. Kim: *Mater. Sci. Eng. A*, 2003, vol. 351A, pp. 183–89.
15. D. Jain, D. Isheim, X.J. Zhang, G. Ghosh, and D.N. Seidman: *Metall. Mater. Trans. A*, 2017, vol. 48A, pp. 3642–54.
16. B.L. Averbach and M. Cohen: *Trans. AIME*, 1948, vol. 179, pp. 401–15.
17. G.E. Hicho, H. Yakowitz, and R.E. Michaelis: *Adv. X-Ray Anal.*, 1971, vol. 14, p. 78.
18. P.W. Fuerschbach and G.R. Eisler: *Trends Weld. Res.: Proc. 6th Int. Conf.*, Phoenix, AZ, USA, April 15–19, 2002, ASM International, Materials Park, OH, 2002, pp. 782–86.
19. G.R. Eisler and P.W. Fuerschbach: *Seventh Int. Conf. Comput. Technol. Weld.*, San Francisco, CA, July 8–11, 1997, National Institute of Standards and Technology, Washington, DC, 1997, pp. 257–68.
20. J.O. Andersson, T. Helander, L. Höglund, P.F. Shi, and B. Sundman: *Calphad*, 2002, vol. 26, pp. 273–312.
21. *Thermo-Calc Software TCFE8 Steels/Fe-Alloys Database Version 8*, Thermo-Calc Software, Stockholm, 2015.
22. M.K. Miller, K.F. Russell, and G.B. Thompson: *Ultramicroscopy*, 2005, vol. 102, pp. 287–98.
23. R.W. Fonda and G. Spanos: *Metall. Mater. Trans. A*, 2014, vol. 45A, pp. 5982–89.
24. R.W. Fonda, G. Spanos, and R.A. Vandermeer: *Scripta Metall. Mater.*, 1994, vol. 31, pp. 683–88.
25. G. Spanos, R.W. Fonda, R.A. Vandermeer, and A. Matuszeski: *Metall. Mater. Trans. A*, 1995, vol. 26A, pp. 3277–93.
26. H. Pous-Romero and H.K.D.H. Bhadeshia: *J. Press. Vessel Technol.*, 2014, vol. 136, p. 031402.
27. J.H. Pak, H.K.D.H. Bhadeshia, and L. Karlsson: *Mater. Sci. Technol.*, 2012, vol. 28, pp. 918–23.
28. J.H. Pak, D.W. Suh, and H.K.D.H. Bhadeshia: *Scripta Mater.*, 2012, vol. 66, pp. 951–53.
29. H.K.D.H. Bhadeshia, E. Keehan, L. Karlsson, and H.O. Andrén: *Trans. Indian Inst. Met.*, 2006, vol. 59, pp. 689–94.
30. J.H. Pak, H.K.D.H. Bhadeshia, L. Karlsson, and E. Keehan: *Sci. Technol. Weld. Join.*, 2008, vol. 13, pp. 593–97.

31. E. Keehan, L. Karlsson, and H.O. Andrén: *Sci. Technol. Weld. Join.*, 2006, vol. 11, pp. 1–8.
32. D.N. Seidman: *Annu. Rev. Mater. Res.*, 2007, vol. 37, pp. 127–58.
33. D.N. Seidman and K. Stiller: *Mater. Res. Soc. Bull.*, 2009, vol. 34, pp. 717–21.
34. O.C. Hellman and D.N. Seidman: *Mater. Sci. Eng.*, 2002, vol. 327, pp. 24–28.
35. O.C. Hellman, J. Vandenbroucke, J. Blatz du Rivage, and D.N. Seidman: *Mater. Sci. Eng.*, 2002, vol. 327, pp. 29–33.
36. D. Isheim, O.C. Hellman, J. Rüsing, and D.N. Seidman: *Interface Sci.*, 2002, vol. 9, pp. 257–64.
37. J. Rüsing, J.T. Sebastian, O.C. Hellman, and D.N. Seidman: *Microsc. Microanal.*, 2000, vol. 6, pp. 445–51.
38. O.C. Hellman, J.A. Vandenbroucke, J. Rüsing, D. Isheim, and D.N. Seidman: *Microsc. Microanal.*, 2000, vol. 6, pp. 437–44.
39. G. Krauss: *Steels: Processing, Structure, and Performance*, 2nd ed., ASM International, Materials Park, OH, 2015, pp. 30–31, 63–73, 338–40.
40. R. Wei, M. Enomoto, R. Hadian, H.S. Zurob, and G.R. Purdy: *Acta Mater.*, 2013, vol. 61, pp. 697–707.
41. S. Watanabe, Y. Ohmori, and T. Kunitake: *Proc. 1st Int. Conf. N. Asp. Martensitic Transform.*, Kobe, JP, May 10–12, 1976, The Japan Institute of Metals, Sendai, JP, 1976, pp. 369–74.
42. B. Fultz, J.I. Kim, Y.H. Kim, and J.W. Morris: *Metall. Trans. A*, 1986, vol. 17A, pp. 967–72.
43. B. Fultz, J.I. Kim, Y.H. Kim, H.J. Kim, G.O. Fior, and J.W. Morris: *Metall. Trans. A*, 1985, vol. 16A, pp. 2237–49.
44. C.A. Apple and G. Krauss: *Acta Metall.*, 1972, vol. 20, pp. 849–56.
45. H. Kessler and W. Pitsch: *Acta Metall.*, 1967, vol. 15, pp. 401–05.
46. Y.K. Lee, H.C. Shin, D.S. Leem, J.Y. Choi, W. Jin, and C.S. Choi: *Mater. Sci. Technol.*, 2003, vol. 19, pp. 393–98.
47. H. Oikawa: *Technol. Rep. Tohoku Univ.*, 1982, vol. 47, pp. 215–24.
48. D.A. Porter, K.E. Easterling, and M.Y. Sherif: *Phase Transformations in Metals and Alloys*, 3rd ed., Taylor and Francis Group, Boca Raton, FL, 2009, pp. 65–98.
49. K.W. Andrews: *J. Iron Steel Inst.*, 1965, vol. 203, pp. 721–27.
50. W. Steven and A.G. Haynes: *J. Iron Steel Inst.*, 1956, vol. 183, pp. 349–59.
51. S. Kou: *Welding Metallurgy*, 2nd ed., Wiley, Hoboken, NJ, 2003, pp. 393–410.
52. E.F. Nippes and J.P. Balaguer: *Weld. J.*, 1986, vol. 65, pp. 237s–43s.
53. X.J. Zhang: NSWCCD, Bethesda, MD, unpublished research, 2016.